
This is an electronic reprint of the original article.
This reprint *may differ* from the original in pagination and typographic detail.

Author(s): Adare, A.; Aidala, C.; Ajitanand, N. N.; Akiba, Y.; Akimoto, R.; Al-Ta'ani, H.; Alexander, J.; Andrews, K. R.; Angerami, A.; Aoki, K.; Kim, Dong Jo; Rak, Jan

Title: Inclusive double-helicity asymmetries in neutral-pion and eta-meson production in $p \rightarrow + p \rightarrow$ collisions at $s = 200\text{GeV}$

Year: 2014

Version:

Please cite the original version:

Adare, A., Aidala, C., Ajitanand, N.N., Akiba, Y., Akimoto, R., Al-Ta'ani, H., Alexander, J., Andrews, K. R., Angerami, A., Aoki, K., Kim, D. J., & Rak, J. (2014). Inclusive double-helicity asymmetries in neutral-pion and eta-meson production in $p \rightarrow + p \rightarrow$ collisions at $s = 200\text{GeV}$. *Physical Review D*, 90(1), Article 012007.
<https://doi.org/10.1103/PhysRevD.90.012007>

All material supplied via JYX is protected by copyright and other intellectual property rights, and duplication or sale of all or part of any of the repository collections is not permitted, except that material may be duplicated by you for your research use or educational purposes in electronic or print form. You must obtain permission for any other use. Electronic or print copies may not be offered, whether for sale or otherwise to anyone who is not an authorised user.

Inclusive double-helicity asymmetries in neutral-pion and eta-meson production in $\vec{p} + \vec{p}$ collisions at $\sqrt{s} = 200$ GeV

A. Adare,¹³ C. Aidala,^{37,42} N. N. Ajitanand,⁵⁹ Y. Akiba,^{54,55} R. Akimoto,¹² H. Al-Ta'ani,⁴⁸ J. Alexander,⁵⁹ K. R. Andrews,¹ A. Angerami,¹⁴ K. Aoki,⁵⁴ N. Apadula,⁶⁰ E. Appelt,⁶⁴ Y. Aramaki,^{12,54} R. Armendariz,⁸ E. C. Aschenauer,⁷ T. C. Awes,⁵⁰ B. Azmoun,⁷ V. Babintsev,²³ M. Bai,⁶ B. Bannier,⁶⁰ K. N. Barish,⁸ B. Bassalleck,⁴⁷ A. T. Basye,¹ S. Bathe,^{5,55} V. Baublis,⁵³ C. Baumann,⁴³ A. Bazilevsky,⁷ R. Belmont,⁶⁴ J. Ben-Benjamin,⁴⁴ R. Bennett,⁶⁰ D. S. Blau,³² J. S. Bok,⁶⁷ K. Boyle,⁵⁵ M. L. Brooks,³⁷ D. Broxmeyer,⁴⁴ H. Buesching,⁷ V. Bumazhnov,²³ G. Bunce,^{7,55} S. Butsyk,³⁷ S. Campbell,⁶⁰ P. Castera,⁶⁰ C.-H. Chen,⁶⁰ C. Y. Chi,¹⁴ M. Chiu,⁷ I. J. Choi,^{24,67} J. B. Choi,¹⁰ R. K. Choudhury,⁴ P. Christiansen,³⁹ T. Chujo,⁶³ O. Chvala,⁸ V. Ciencialo,⁵⁰ Z. Citron,⁶⁰ B. A. Cole,¹⁴ Z. Conesa del Valle,³⁴ M. Connors,⁶⁰ M. Csanád,¹⁷ T. Csörgő,⁶⁶ S. Dairaku,^{33,54} A. Datta,⁴¹ G. David,⁷ M. K. Dayananda,²⁰ A. Denisov,²³ A. Deshpande,^{55,60} E. J. Desmond,⁷ K. V. Dharmawardane,⁴⁸ O. Dietzsch,⁵⁷ A. Dion,^{27,60} M. Donadelli,⁵⁷ O. Drapier,³⁴ A. Drees,⁶⁰ K. A. Drees,⁶ J. M. Durham,^{37,60} A. Durum,²³ L. D'Orazio,⁴⁰ Y. V. Efremenko,⁵⁰ T. Engelmores,¹⁴ A. Enokizono,⁵⁰ H. En'yo,^{54,55} S. Esumi,⁶³ B. Fadem,⁴⁴ D. E. Fields,⁴⁷ M. Finger,⁹ M. Finger, Jr.,⁹ F. Fleuret,³⁴ S. L. Fokin,³² J. E. Frantz,⁴⁹ A. Franz,⁷ A. D. Frawley,¹⁹ Y. Fukao,⁵⁴ T. Fusayasu,⁴⁶ C. Gal,⁶⁰ I. Garishvili,⁶¹ F. Giordano,²⁴ A. Glenn,³⁶ X. Gong,⁵⁹ M. Gonin,³⁴ Y. Goto,^{54,55} R. Granier de Cassagnac,³⁴ N. Grau,^{2,14} S. V. Greene,⁶⁴ M. Grosse Perdekamp,²⁴ T. Gunji,¹² L. Guo,³⁷ H.-Å. Gustafsson,^{39,*} J. S. Haggerty,⁷ K. I. Hahn,¹⁸ H. Hamagaki,¹² J. Hamblen,⁶¹ R. Han,⁵² J. Hanks,¹⁴ C. Harper,⁴⁴ K. Hashimoto,^{54,56} E. Haslum,³⁹ R. Hayano,¹² X. He,²⁰ T. K. Hemmick,⁶⁰ T. Hester,⁸ J. C. Hill,²⁷ R. S. Hollis,⁸ W. Holzmann,¹⁴ K. Homma,²² B. Hong,³¹ T. Horaguchi,⁶³ Y. Hori,¹² D. Hornback,⁵⁰ J. Huang,^{7,37} S. Huang,⁶⁴ T. Ichihara,^{54,55} R. Ichimiya,⁵⁴ H. Iinuma,³⁰ Y. Ikeda,⁶³ K. Imai,^{28,33,54} M. Inaba,⁶³ A. Iordanova,⁸ D. Isenhowe,¹ M. Ishihara,⁵⁴ M. Issah,⁶⁴ D. Ivanischev,⁵³ Y. Iwanaga,²² B. V. Jacak,⁶⁰ J. Jia,^{7,59} X. Jiang,³⁷ D. John,⁶¹ B. M. Johnson,⁷ T. Jones,¹ K. S. Joo,⁴⁵ D. Jouan,⁵¹ J. Kamin,⁶⁰ S. Kaneti,⁶⁰ B. H. Kang,²¹ J. H. Kang,⁶⁷ J. S. Kang,²¹ J. Kapustinsky,³⁷ K. Karatsu,^{33,54} M. Kasai,^{54,56} D. Kaway,^{41,55} A. V. Kazantsev,³² T. Kempel,²⁷ A. Khanzadeev,⁵³ K. M. Kijima,²² B. I. Kim,³¹ D. J. Kim,²⁹ E.-J. Kim,¹⁰ Y.-J. Kim,²⁴ Y. K. Kim,²¹ E. Kinney,¹³ Á. Kiss,¹⁷ E. Kistenev,⁷ D. Kleinjan,⁸ P. Kline,⁶⁰ L. Kochenda,⁵³ B. Komkov,⁵³ M. Konno,⁶³ J. Koster,²⁴ D. Kotov,⁵³ A. Král,¹⁵ G. J. Kunde,³⁷ K. Kurita,^{54,56} M. Kurosawa,⁵⁴ Y. Kwon,⁶⁷ G. S. Kyle,⁴⁸ R. Lacey,⁵⁹ Y. S. Lai,¹⁴ J. G. Lajoie,²⁷ A. Lebedev,²⁷ D. M. Lee,³⁷ J. Lee,¹⁸ K. B. Lee,³¹ K. S. Lee,³⁷ S. H. Lee,⁶⁰ S. R. Lee,¹⁰ M. J. Leitch,³⁷ M. A. L. Leite,⁵⁷ X. Li,¹¹ S. H. Lim,⁶⁷ L. A. Linden Levy,¹³ H. Liu,³⁷ M. X. Liu,³⁷ B. Love,⁶⁴ D. Lynch,⁷ C. F. Maguire,⁶⁴ Y. I. Makdisi,⁶ A. Manion,⁶⁰ V. I. Manko,³² E. Mannel,¹⁴ Y. Mao,^{52,54} H. Masui,⁶³ M. McCumber,^{13,60} P. L. McGaughey,³⁷ D. McGlinchey,^{13,19} C. McKinney,²⁴ N. Means,⁶⁰ M. Mendoza,⁸ B. Meredith,²⁴ Y. Miake,⁶³ T. Mibe,³⁰ A. C. Mignerey,⁴⁰ K. Miki,^{54,63} A. Milov,⁶⁵ J. T. Mitchell,⁷ Y. Miyachi,^{54,62} A. K. Mohanty,⁴ H. J. Moon,⁴⁵ Y. Morino,¹² A. Morreale,⁸ D. P. Morrison,^{7,†} S. Motschwiller,⁴⁴ T. V. Moukhanova,³² T. Murakami,³³ J. Murata,^{54,56} S. Nagamiya,³⁰ J. L. Nagle,^{13,‡} M. Naglis,⁶⁵ M. I. Nagy,⁶⁶ I. Nakagawa,^{54,55} Y. Nakamiya,²² K. R. Nakamura,^{33,54} T. Nakamura,⁵⁴ K. Nakano,⁵⁴ J. Newby,³⁶ M. Nguyen,⁶⁰ M. Nihashi,²² R. Nouicer,⁷ A. S. Nyanin,³² C. Oakley,²⁰ E. O'Brien,⁷ C. A. Ogilvie,²⁷ M. Oka,⁶³ K. Okada,⁵⁵ A. Oskarsson,³⁹ M. Ouchida,^{22,54} K. Ozawa,¹² R. Pak,⁷ V. Pantuev,^{25,60} V. Papavassiliou,⁴⁸ B. H. Park,²¹ I. H. Park,¹⁸ S. K. Park,³¹ S. F. Pate,⁴⁸ L. Patel,²⁰ H. Pei,²⁷ J.-C. Peng,²⁴ H. Pereira,¹⁶ D. Yu. Peressounko,³² R. Petti,⁶⁰ C. Pinkenburg,⁷ R. P. Pisani,⁷ M. Proissl,⁶⁰ M. L. Purschke,⁷ H. Qu,²⁰ J. Rak,²⁹ I. Ravinovich,⁶⁵ K. F. Read,^{50,61} K. Reygers,⁴³ V. Riabov,⁵³ Y. Riabov,⁵³ E. Richardson,⁴⁰ D. Roach,⁶⁴ G. Roche,³⁸ S. D. Rolnick,⁸ M. Rosati,²⁷ S. S. E. Rosendahl,³⁹ B. Sahlmueller,^{43,60} N. Saito,³⁰ T. Sakaguchi,⁷ V. Samsonov,⁵³ S. Sano,²³ M. Sarsour,²⁰ T. Sato,⁶³ M. Savastio,⁶⁰ S. Sawada,³⁰ K. Sedgwick,⁸ R. Seidl,⁵⁵ R. Seto,⁸ D. Sharma,⁶⁵ I. Shein,²³ T.-A. Shibata,^{54,62} K. Shigaki,²² H. H. Shim,³¹ M. Shimomura,⁶³ K. Shoji,^{33,54} P. Shukla,⁴ A. Sickles,⁷ C. L. Silva,²⁷ D. Silvermyr,⁵⁰ C. Silvestre,¹⁶ K. S. Sim,³¹ B. K. Singh,³ C. P. Singh,³ V. Singh,³ M. Slunečka,⁹ T. Sodre,⁴⁴ R. A. Soltz,³⁶ W. E. Sondheim,³⁷ S. P. Sorensen,⁶¹ I. V. Sourikova,⁷ P. W. Stankus,⁵⁰ E. Stenlund,³⁹ S. P. Stoll,⁷ T. Sugitate,²² A. Sukhanov,⁷ J. Sun,⁶⁰ J. Sziklai,⁶⁶ E. M. Takagui,⁵⁷ A. Takahara,¹² A. Taketani,^{54,55} R. Tanabe,⁶³ Y. Tanaka,⁴⁶ S. Taneja,⁶⁰ K. Tanida,^{58,33,54} M. J. Tannenbaum,⁷ S. Tarafdar,³ A. Taranenko,⁵⁹ E. Tennant,⁴⁸ H. Themann,⁶⁰ D. Thomas,¹ M. Togawa,⁵⁵ L. Tomášek,²⁶ M. Tomášek,²⁶ H. Torii,²² R. S. Towell,¹ I. Tseruya,⁶⁵ Y. Tsuchimoto,²² K. Utsunomiya,¹² C. Vale,⁷ H. W. van Hecke,³⁷ E. Vazquez-Zambrano,¹⁴ A. Veicht,¹⁴ J. Velkovska,⁶⁴ R. Vértesi,⁶⁶ M. Virius,¹⁵ A. Vossen,²⁴ V. Vrba,²⁶ E. Vznuzdaev,⁵³ X. R. Wang,⁴⁸ D. Watanabe,²² K. Watanabe,⁶³ Y. Watanabe,^{54,55} Y. S. Watanabe,¹² F. Wei,²⁷ R. Wei,⁵⁹ J. Wessels,⁴³ S. N. White,⁷ D. Winter,¹⁴ C. L. Woody,¹³ R. M. Wright,¹ M. Wysocki,¹³ Y. L. Yamaguchi,^{12,54} R. Yang,²⁴ A. Yanovich,²³ J. Ying,²⁰ S. Yokkaichi,^{54,55} J. S. Yoo,¹⁸ Z. You,^{37,52} G. R. Young,⁵⁰ I. Younus,^{35,47} I. E. Yushmanov,³² W. A. Zajc,¹⁴ A. Zelenski,⁶ and S. Zhou¹¹

(PHENIX Collaboration)

¹Abilene Christian University, Abilene, Texas 79699, USA²Department of Physics, Augustana College, Sioux Falls, South Dakota 57197, USA

- ³Department of Physics, Banaras Hindu University, Varanasi 221005, India
⁴Bhabha Atomic Research Centre, Bombay 400 085, India
⁵Baruch College, City University of New York, New York, New York 10010, USA
⁶Collider-Accelerator Department, Brookhaven National Laboratory, Upton, New York 11973-5000, USA
⁷Physics Department, Brookhaven National Laboratory, Upton, New York 11973-5000, USA
⁸University of California–Riverside, Riverside, California 92521, USA
⁹Charles University, Ovocný trh 5, Praha 1, 116 36, Prague, Czech Republic
¹⁰Chonbuk National University, Jeonju 561-756, Korea
¹¹Science and Technology on Nuclear Data Laboratory, China Institute of Atomic Energy, Beijing 102413, People's Republic of China
¹²Center for Nuclear Study, Graduate School of Science, University of Tokyo, 7-3-1 Hongo, Bunkyo, Tokyo 113-0033, Japan
¹³University of Colorado, Boulder, Colorado 80309, USA
¹⁴Columbia University, New York, New York 10027, USA and Nevis Laboratories, Irvington, New York 10533, USA
¹⁵Czech Technical University, Zikova 4, 166 36 Prague 6, Czech Republic
¹⁶Dapnia, CEA Saclay, F-91191 Gif-sur-Yvette, France
¹⁷ELTE, Eötvös Loránd University, H-1117 Budapest, Pázmány Péter sétány 1/A, Hungary
¹⁸Ewha Womans University, Seoul 120-750, Korea
¹⁹Florida State University, Tallahassee, Florida 32306, USA
²⁰Georgia State University, Atlanta, Georgia 30303, USA
²¹Hanyang University, Seoul 133-792, Korea
²²Hiroshima University, Kagamiyama, Higashi-Hiroshima 739-8526, Japan
²³IHEP Protvino, State Research Center of Russian Federation, Institute for High Energy Physics, Protvino 142281, Russia
²⁴University of Illinois at Urbana-Champaign, Urbana, Illinois 61801, USA
²⁵Institute for Nuclear Research of the Russian Academy of Sciences, prospekt 60-letiya Oktyabrya 7a, Moscow 117312, Russia
²⁶Institute of Physics, Academy of Sciences of the Czech Republic, Na Slovance 2, 182 21 Prague 8, Czech Republic
²⁷Iowa State University, Ames, Iowa 50011, USA
²⁸Advanced Science Research Center, Japan Atomic Energy Agency, 2-4 Shirakata Shirane, Tokai-mura, Naka-gun, Ibaraki-ken 319-1195, Japan
²⁹Helsinki Institute of Physics and University of Jyväskylä, P.O. Box 35, FI-40014 Jyväskylä, Finland
³⁰KEK, High Energy Accelerator Research Organization, Tsukuba, Ibaraki 305-0801, Japan
³¹Korea University, Seoul 136-701, Korea
³²Russian Research Center “Kurchatov Institute”, Moscow 123098, Russia
³³Kyoto University, Kyoto 606-8502, Japan
³⁴Laboratoire Leprince-Ringuet, Ecole Polytechnique, CNRS-IN2P3, Route de Saclay, F-91128, Palaiseau, France
³⁵Physics Department, Lahore University of Management Sciences, Lahore 54792, Pakistan
³⁶Lawrence Livermore National Laboratory, Livermore, California 94550, USA
³⁷Los Alamos National Laboratory, Los Alamos, New Mexico 87545, USA
³⁸LPC, Université Blaise Pascal, CNRS-IN2P3, Clermont-Fd, 63177 Aubiere Cedex, France
³⁹Department of Physics, Lund University, Box 118, SE-221 00 Lund, Sweden
⁴⁰University of Maryland, College Park, Maryland 20742, USA
⁴¹Department of Physics, University of Massachusetts, Amherst, Massachusetts 01003-9337, USA
⁴²Department of Physics, University of Michigan, Ann Arbor, Michigan 48109-1040, USA
⁴³Institut für Kernphysik, University of Muenster, D-48149 Muenster, Germany
⁴⁴Muhlenberg College, Allentown, Pennsylvania 18104-5586, USA
⁴⁵Myongji University, Yongin, Kyonggido 449-728, Korea
⁴⁶Nagasaki Institute of Applied Science, Nagasaki-shi, Nagasaki 851-0193, Japan
⁴⁷University of New Mexico, Albuquerque, New Mexico 87131, USA
⁴⁸New Mexico State University, Las Cruces, New Mexico 88003, USA
⁴⁹Department of Physics and Astronomy, Ohio University, Athens, Ohio 45701, USA
⁵⁰Oak Ridge National Laboratory, Oak Ridge, Tennessee 37831, USA
⁵¹IPN-Orsay, Université Paris Sud, CNRS-IN2P3, BP1, F-91406 Orsay, France
⁵²Peking University, Beijing 100871, People's Republic of China
⁵³PNPI, Petersburg Nuclear Physics Institute, Gatchina, Leningrad region 188300, Russia
⁵⁴RIKEN Nishina Center for Accelerator-Based Science, Wako, Saitama 351-0198, Japan

⁵⁵*RIKEN BNL Research Center, Brookhaven National Laboratory, Upton, New York 11973-5000, USA*⁵⁶*Physics Department, Rikkyo University, 3-34-1 Nishi-Ikebukuro, Toshima, Tokyo 171-8501, Japan*⁵⁷*Universidade de São Paulo, Instituto de Física, Caixa Postal 66318, São Paulo CEP05315-970, Brazil*⁵⁸*Seoul National University, Seoul 151-742, Korea*⁵⁹*Chemistry Department, Stony Brook University, SUNY, Stony Brook, New York 11794-3400, USA*⁶⁰*Department of Physics and Astronomy, Stony Brook University, SUNY, Stony Brook, New York 11794-3800, USA*⁶¹*University of Tennessee, Knoxville, Tennessee 37996, USA*⁶²*Department of Physics, Tokyo Institute of Technology, Oh-okayama, Meguro, Tokyo 152-8551, Japan*⁶³*Institute of Physics, University of Tsukuba, Tsukuba, Ibaraki 305, Japan*⁶⁴*Vanderbilt University, Nashville, Tennessee 37235, USA*⁶⁵*Weizmann Institute, Rehovot 76100, Israel*⁶⁶*Institute for Particle and Nuclear Physics, Wigner Research Centre for Physics, Hungarian Academy of Sciences (Wigner RCP, RMKI) H-1525 Budapest 114, P.O. Box 49, Budapest, Hungary*⁶⁷*Yonsei University, IPAP, Seoul 120-749, Korea*

(Received 25 February 2014; published 17 July 2014)

Results are presented from data recorded in 2009 by the PHENIX experiment at the Relativistic Heavy Ion Collider for the double-longitudinal spin asymmetry, A_{LL} , for π^0 and η production in $\sqrt{s} = 200$ GeV polarized $p + p$ collisions. Comparison of the π^0 results with different theory expectations based on fits of other published data showed a preference for small positive values of gluon polarization, ΔG , in the proton in the probed Bjorken x range. The effect of adding the new 2009 π^0 data to a recent global analysis of polarized scattering data is also shown, resulting in a best fit value $\Delta G_{\text{DSSV}}^{[0.05,0.2]} = 0.06_{-0.15}^{+0.11}$ in the range $0.05 < x < 0.2$, with the uncertainty at $\Delta\chi^2 = 9$ when considering only statistical experimental uncertainties. Shifting the PHENIX data points by their systematic uncertainty leads to a variation of the best-fit value of $\Delta G_{\text{DSSV}}^{[0.05,0.2]}$ between 0.02 and 0.12, demonstrating the need for full treatment of the experimental systematic uncertainties in future global analyses.

DOI: 10.1103/PhysRevD.90.012007

PACS numbers: 13.85.Ni, 13.88.+e, 14.20.Dh, 25.75.Dw

I. INTRODUCTION

The proton has a finite charge radius and can be described as a collection of fermionic quarks whose interaction is mediated by bosonic gluons. The proton is also a spin-1/2 fermion itself, which constrains the total angular momentum of these constituents and has been described in several proposed sum rules [1–5]. In the infinite momentum frame, all possible contributions to the proton spin can be classified according to the Manohar-Jaffe sum rule [1],

$$S_p = \frac{1}{2} = \frac{1}{2}\Delta\Sigma + \Delta G + L_q + L_g, \quad (1)$$

which makes explicit the contributions from quark and gluon spin ($\Delta\Sigma$ and ΔG , respectively) and orbital angular momentum (L_q and L_g , respectively).

Early experiments discovered that the $\frac{1}{2}\Delta\Sigma$ term falls far short of the total [6–8]. Current knowledge from global fits [9–13] of polarized deep inelastic scattering (DIS) and

semi-inclusive DIS (SIDIS) data [7,8,14,15] puts the contribution at only 25%–35% of the proton spin, depending on the assumptions used, including whether SU(3) symmetry is enforced. This realization provided the motivation to study the ΔG term by colliding longitudinally polarized protons at the Relativistic Heavy Ion Collider (RHIC), including the results presented here.

Polarized proton collisions at RHIC allow access to ΔG at leading order (LO) in perturbative quantum chromodynamics (pQCD), unlike lepton-hadron scattering experiments that are only sensitive to ΔG via photon-gluon fusion at next-to-leading order (NLO) in pQCD or via momentum-transfer-scaling violations of the polarized structure function g_1 . RHIC experiments make the connection to ΔG via inclusive double-helicity asymmetries, A_{LL} , defined by

$$A_{LL} = \frac{\Delta\sigma}{\sigma} = \frac{\sigma_{++} - \sigma_{+-}}{\sigma_{++} + \sigma_{+-}}. \quad (2)$$

Here, σ ($\Delta\sigma$) is the (polarized) cross section for a given observable, and “++” (“+-”) signifies $\vec{p} + \vec{p}$ collisions with the same (opposite) helicity. Within the framework of pQCD, A_{LL} can also be “factorized” to make the parton spin contributions explicit:

*Deceased.

†PHENIX Co-Spokesperson.
morrisson@bnl.gov‡PHENIX Co-Spokesperson.
jamie.nagle@colorado.edu

$$A_{LL} = \frac{\sum_{abc} \Delta f_a(x_1, \mu_F^2) \otimes \Delta f_b(x_2, \mu_F^2) \otimes \Delta \sigma^{a+b \rightarrow c+X}(x_1, x_2, p_c, \mu_F^2, \mu_R^2, \mu_{FF}^2) \otimes D_c^h(z, \mu_{FF}^2)}{\sum_{abc} f_a(x_1, \mu_F^2) \otimes f_b(x_2, \mu_F^2) \otimes \sigma^{a+b \rightarrow c+X}(x_1, x_2, p_c, \mu_F^2, \mu_R^2, \mu_{FF}^2) \otimes D_c^h(z, \mu_{FF}^2)}, \quad (3)$$

where $f_{a,b}$ ($\Delta f_{a,b}$) are the unpolarized (polarized) parton distribution functions [PDF (pPDF)], phenomenological functions describing the statistical distribution for partons a, b (gluons, quarks, or antiquarks) in a proton as a function of the momentum fraction Bjorken x . D_c^h is the fragmentation function (FF) describing the probability for a parton c with momentum p_c to fragment into a hadron h with momentum p_h and thus with a given $z = p_h/p_c$. $\Delta \sigma^{a+b \rightarrow c+X}$ and $\sigma^{a+b \rightarrow c+X}$ are the polarized and unpolarized partonic cross sections, respectively, and are calculable in pQCD. Factorization, renormalization and fragmentation scales μ_F , μ_R and μ_{FF} are used to separate the perturbative and nonperturbative parts. The diagram in Fig. 1 summarizes the components of pQCD factorization. The theoretical calculations discussed in this paper with respect to our results are performed at NLO in pQCD.

To test the applicability of NLO pQCD to our A_{LL} results, PHENIX has previously published π^0 - and η -meson cross sections [16,17]. These cross sections, along with others at $\sqrt{s} = 200$ GeV for jets [18] and direct photons [19], are well described by the theory within its uncertainties, based on the method of varying the choice of scales by a factor of 2. In our previous publication [20], we examined the impact of this theoretical scale uncertainty with respect to our $A_{LL}^{\pi^0}$ results, and found that it is important and should be considered in future global analyses.

A number of different channels can be used to access the gluon polarization using Eq. (3), including a final state hadron or jet, as well as rarer probes such as direct photon and heavy flavor [21]. The latter of these are produced through fewer processes, which allows for a simple leading-order interpretation of the results. Jets or low-mass hadrons such as pions are not as readily interpretable due to the multiple QCD processes through which they are produced, but they have significantly higher production rates. PHENIX results for $A_{LL}^{\pi^0}$ [16,20,22] and results for jet

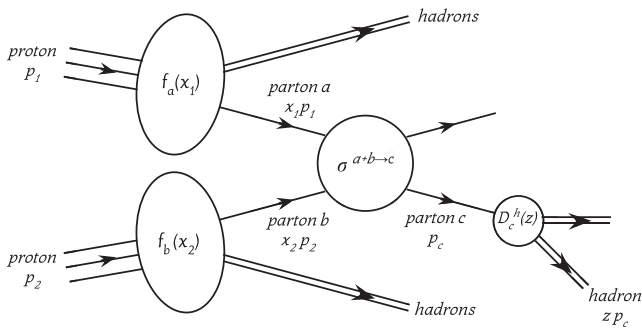


FIG. 1. Diagram showing the three elements of pQCD factorization: parton distribution functions $f_{a,b}(x)$, partonic cross sections $\sigma^{a+b \rightarrow c}$, and fragmentation functions $D_c^h(z)$.

A_{LL} from the STAR experiment at RHIC [18,23] have ruled out large values of ΔG but are still consistent with a range of assumptions, including fixing the polarized PDF for the gluon, $\Delta g(x, \mu^2)$, to zero at an NLO input scale of $\mu^2 = 0.40$ GeV². The constraining power of these results has been quantified via inclusion in a global fit of polarized DIS and semi-inclusive DIS results by de Florian *et al.* (DSSV) [9,10], resulting in an integral $\Delta G_{\text{DSSV08}}^{[0.05,0.2]} = 0.005^{+0.129}_{-0.164}$ in the Bjorken- x range [0.05,0.2]. As detailed in [20], the full x range probed by the PHENIX $A_{LL}^{\pi^0}$ measurements is [0.02,0.3].

The A_{LL}^{η} has also been measured [17], but it has not yet been used in global fits. One reason for this is that existing $e^+ + e^-$ data does not constrain η fragmentation functions as well as those for the pions [24,25]. However, PHENIX has released results for the η/π^0 cross section ratio in $p + p$ collisions [17,26] with systematic uncertainties much smaller than on either cross section measurement alone. Future inclusion of this ratio in global fits could be used to circumvent this issue with the fragmentation functions.

In this paper, we present measurements of A_{LL} in π^0 - and η -meson production in longitudinally polarized $p + p$ collisions at $\sqrt{s} = 200$ GeV, based on data collected in 2009, which approximately doubles the statistics in the $\sqrt{s} = 200$ GeV PHENIX neutral meson A_{LL} data set [17,20] and extends the measured p_T range. Descriptions of RHIC and the PHENIX experiment are laid out in Sec. II, followed by a detailed account of the analysis procedure in Sec. III including discussion of the systematic uncertainties. Finally, in Secs. IV and V, we show our final results and discuss them in relation to global analyses of polarized scattering data.

II. EXPERIMENTAL SETUP

A. Polarized beams at RHIC

RHIC comprises two counterrotating storage rings, designated blue and yellow, in each of which as many as 120 polarized proton bunches of 10^{11} protons or more can be accelerated to an energy of 255 GeV per proton. In the 2009 run, RHIC was typically operated with 109 filled bunches in each ring. The rings intersect in six locations such that the bunches collide with a one-to-one correspondence. This allows an unambiguous definition of 120 “crossings” per revolution at each experiment, with a 106 ns separation. At PHENIX, there were 107 crossings in which both bunches were filled and four crossings with only the bunch in one ring filled to enable study of beam background.

Outside of the experimental interaction regions, the stable polarization direction in RHIC is vertical [27].

The polarization for each bunch can be aligned or anti-aligned with this vertical axis at injection, allowing for variation over all four possible polarization combinations within four crossings, or 424 ns. To cancel false asymmetries related to coupling between the polarization patterns and the bunch/crossing structure, four different polarization vs bunch patterns, hereafter referred to as “spin patterns,” were used, defined by changing the sign of all polarizations in one or both beams from the base pattern. The patterns were cycled after each successful beam store, or “fill.”

Determination of the beam polarizations required combining measurements from two separate polarimeters. First, the relative beam polarizations were measured several times per fill using a fast, high-statistics relative polarimeter, which detects elastic scattering off of a thin carbon target that is moved across the beam. This polarimeter can determine both the relative magnitude of the polarization and any variation across the width of the beam [28]. This measurement was normalized by comparing its average over the entire data set to the average of an absolute polarization measurement from the second polarimeter, which is based on scattering of the beam with a continuously running polarized hydrogen gas-jet target [29]. For 2009 $\sqrt{s} = 200$ GeV running, the average beam polarizations were $P_B = 0.56$ for the blue beam and $P_Y = 0.55$ for the yellow beam, for a product $P_B P_Y = 0.31$. The overall relative scale uncertainty on the product $P_B P_Y$ was 6.5%, with 4.8% of that considered correlated with the polarization uncertainties from RHIC runs in 2005 and 2006 [30].

B. The PHENIX experiment

The PHENIX detector [31] comprises two forward muon arms and two central arms, shown in Fig. 2. Except for luminosity normalization using counters at forward

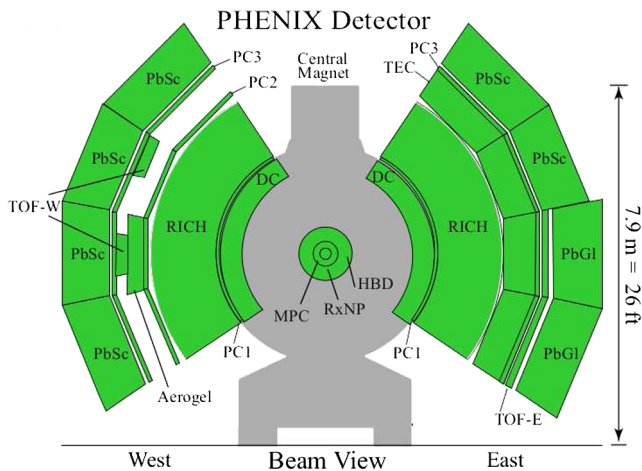


FIG. 2 (color online). Cross section of the PHENIX central arms in their 2009–2010 configuration. The EMCal (PbSc and PbGl) is the primary subsystem used in this analysis. The PC3 is also used to veto charged particles. Not pictured in this view are the BBC and ZDC luminosity monitors at forward rapidity.

rapidity, the present analysis uses only the central arms, each of which cover a pseudorapidity range of $|\eta| < 0.35$ and have azimuthal coverage of $\Delta\phi = \frac{\pi}{2}$. The PHENIX central magnet comprises two coils which provide a field integral of up to 1.15 Tm in $|\eta| < 0.35$ when they are run with the same polarity, as was done in 2005 and 2006. In 2009, the two central coils were run with opposite polarity to create a field-free region near the beam pipe for the newly installed hadron-blind detector [32], which is not used in the present analysis and has a negligible effect on π^0 - and η -meson decays as a conversion material. From a radius of 2–5 m, which is outside the magnetic field region, there are several tracking and particle-identification detectors that are not used in this analysis. At a radius of approximately 5 m, there is a thin multiwire proportional chamber called the pad chamber (PC3) followed immediately by an electromagnetic calorimeter (EMCal), both of which are used in this analysis.

1. EMCal

Neutral pion and eta mesons can both be analyzed via their diphoton decay channel (for the π^0 , the branching ratio is 99%, for the η , 39% [33]), which allows for accurate reconstruction of both mesons using a sufficiently segmented electromagnetic calorimeter. The PHENIX EMCal employs two separate technologies to have sensitivity to calorimeter-based systematic effects. Six out of the eight EMCal sectors are lead scintillator (PbSc), which are Shashlik calorimeters based on scintillation calorimetry, while the remaining two are lead glass (PbGl), which are based on Čerenkov radiation calorimetry, which makes them significantly less responsive to hadrons.

Both the PbSc and PbGl are designed to measure the total energy of an electromagnetic shower, with active depths of 18.8 and 14.3 radiation lengths, respectively. The nominal energy resolutions from test-beam data are $8.1\%/\sqrt{E[\text{GeV}]} \oplus 2.1\%$ and $6.0\%/\sqrt{E[\text{GeV}]} \oplus 0.9\%$ [34].

The PbSc (PbGl) also have sufficient lateral tower segmentation, $\Delta\eta \sim 0.01(0.008)$ and $\Delta\phi \sim 0.01(0.008)$ rad, to measure not only the position, but also the transverse distribution of an electromagnetic shower, with a typical shower contained in a 3×3 array of EMCal towers. The segmentation is also sufficient to avoid pile-up at the highest RHIC $p + p$ rates and in the high-multiplicity environment of heavy ion collisions.

The relative time-of-flight (ToF) for showers can also be measured with the EMCal with a timing resolution of about 0.7 ns for the present data. This measurement can be used to reduce the contribution from hadrons and other backgrounds that are out of time from the expected arrival for a photon.

2. EMCal trigger

To record a significant sample of events containing a π^0 or η meson with large transverse momentum (p_T), a high energy photon trigger is used. A trigger tile is defined as a

2×2 array of EMCal towers, and, for the present analysis, the energy in a 2×2 array of tiles (or 4×4 towers) is summed and compared to the trigger threshold. To reduce loss at the edge of a tile, these groups of 4×4 towers overlap. For this analysis, we use two trigger thresholds, one at 1.4 GeV and one at 2.1 GeV. For diphoton decays, these are maximally efficient at parent meson energies of > 4 GeV and > 6 GeV, respectively. Since the reset time of the trigger, ~ 140 ns, is longer than the ~ 106 ns between bunches, two separate trigger circuits are used to read out even- and odd-numbered crossings. This can lead to variations in the effective thresholds in even and odd crossings, requiring the analysis to be done separately for each.

3. PC3

The PC3 provides nonprojective tracking via a pixelated cathode that is segmented into $16.8 \text{ mm} \times 16.8 \text{ mm}$ pads, giving it excellent spatial resolution. This detector is used in the present analyses only as a veto for charged particle clusters, as described in Sec. III A 1.

4. Luminosity monitors

PHENIX has two luminosity monitors with which to normalize the luminosity variations between same and opposite helicity bunch crossings. The main luminosity monitor is the beam-beam counter (BBC) [31], which comprises two arms located $|z| = 144$ cm from the interaction point (IP) along the beam axis, covering a pseudorapidity range of $3.1 < |\eta| < 3.9$. Each arm has 64 quartz crystal Čerenkov radiators attached to photomultiplier tubes. The BBC also functions as the minimum-bias (MB) collision trigger for this data set, with a requirement that at least one photomultiplier tube fire in each arm and that the timing of the hits reconstructs to a collision with a z vertex within 30 cm of the nominal IP. The yield of MB triggers in crossings where the data acquisition system was ready to take data was used to determine the luminosity.

The second luminosity monitor, the zero-degree calorimeter (ZDC) [31], comprises two arms located $|z| = 18$ m from the IP along the beam axis, covering $|\eta| > 6$. Each arm is composed of three sections of hadron calorimeter composed of optical fibers for Čerenkov sampling sandwiched between layers of tungsten absorber. The three sections constitute a total of five nuclear interaction lengths. As the arms lie beyond the bending magnets, which serve to separate the two beams outside the experimental area but also sweep away charged particles from the interaction, the ZDC primarily triggers on neutrals. A ZDC trigger requires a minimum energy deposit in each arm of nominally 20 GeV.

5. Local polarimeter

The A_{LL} measurements require longitudinal polarization. Four spin rotator magnets (two in each ring) located outside of the PHENIX interaction region rotate the beam

polarization from the stable vertical direction to the longitudinal direction before the IP and back to vertical afterward. A position-sensitive shower-maximum detector, composed of vertical and horizontal scintillator strips, is located between the first and second sections in each ZDC arm. It is used in conjunction with the ZDC to measure an azimuthal asymmetry in forward neutron production with a magnitude of 0.07 [35] during transverse polarization running (with the spin rotators turned off). This asymmetry should vanish when the beam polarization vector is perfectly longitudinal. The size of the residual asymmetry can therefore be used to determine the remaining transverse component, and thus the degree of effective longitudinal polarization. In 2009 at $\sqrt{s} = 200$ GeV, the fraction of the polarization along the longitudinal direction in the blue beam was $0.994^{+0.006}_{-0.008}(\text{stat})^{+0.003}_{-0.010}(\text{syst})$ and in the yellow beam $0.974^{+0.014}_{-0.018}(\text{stat})^{+0.019}_{-0.035}(\text{syst})$.

III. DATA ANALYSIS

A. Event and photon selection

Events used in this analysis require a MB trigger in coincidence with a high energy trigger in the EMCal. An off-line vertex cut is applied, which requires that the vertex reconstructed using the BBC be within $|z| = 30$ cm of the nominal IP. On the order of two billion events passing this off-line cut were analyzed.

Photon candidates are selected from all energy deposit clusters in the EMCal. A minimum energy of 100 MeV in PbSc and 200 MeV in PbGl is required to reduce the impact of noise in the detector. Clusters centered on towers that are markedly noisy or dead, or centered on towers neighboring a markedly noisy or dead tower, are discarded. Clusters centered within two towers of the edge of each EMCal sector's acceptance are also excluded.

A major source of background in the photon candidate sample are charged hadrons, which are removed by three cuts based on shower shape, time of flight (ToF) and association with hits in the PC3. For the shower shape cut, the distribution among towers of the total energy deposited is compared with the expected distribution for an electromagnetic shower, based on results from test beam data. The resulting cut is 98% efficient for photons. The other two cuts are discussed in more detail below.

Also of concern is background of clusters from previous events; since they can be from crossings with a different bunch helicity combination, the asymmetries are affected. Photons from meson decays in previous events are effectively removed by the trigger requirement described in Sec. III B. The ToF cut is effective in targeting the remaining clusters of this type.

1. Charge veto cut

One method to remove charged hadrons is to veto photon candidates with associated (charged particle) hits in

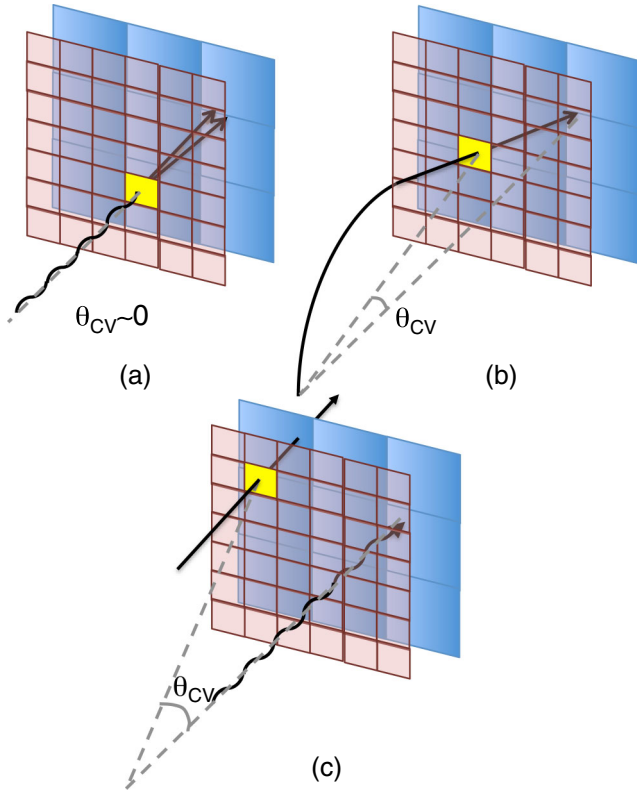


FIG. 3 (color online). Schematic (not to scale) of the hits in the PC3 (transparent grid) and the related θ_{CV} from three particle classes, which leave clusters in the EMCAL (solid grid behind PC3): (a) photons that convert outside of the magnetic field prior to the EMCAL, and have very small θ_{CV} , (b) charged hadrons that bend in the magnetic field, and so have moderate sized θ_{CV} , and (c) photons that do not convert, and are randomly associated with a different particle's PC3 hit, and therefore are likely to have large θ_{CV} .

the PC3. However, to not unnecessarily remove real photons that pair converted before the EMCAL, but outside of the magnetic field, a two-sided cut was developed.

We define two vectors: (1) the vector starting at the event vertex and pointing to a cluster in the EMCAL and (2) the vector pointing from the vertex to the hit in the PC3 nearest to the EMCAL cluster. The angle between these vectors is defined as θ_{CV} , the charge veto angle. The diagram in Fig. 3 shows schematically how this angle is defined for three distinct cases, which can be classified according to the relative magnitude of θ_{CV} :

- (1) Small θ_{CV} : e^+e^- pairs from photon conversions outside of the magnetic field region can still form a single cluster if their opening angle or the conversion's distance from the EMCAL is small. In this case we may find an associated PC3 hit directly in front of the cluster, but we can still reconstruct the original photon from the energy deposited. Thus we should retain clusters with small θ_{CV} .
- (2) Moderate θ_{CV} : Due to the separation between the PC3 and EMCAL as well as the large EMCAL

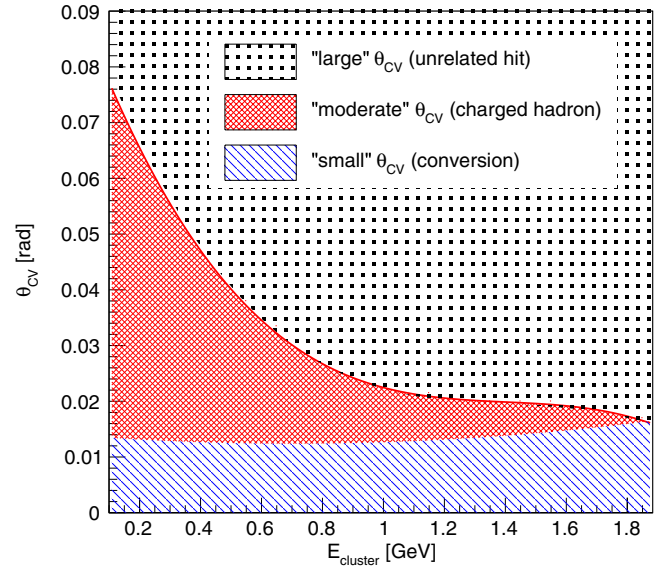


FIG. 4 (color online). θ_{CV} intervals used in the analysis as a function of cluster energy in the EMCAL PbSc. Clusters in the red cross-hatched region are excluded from the analysis. For $E_{\text{cluster}} > 1.9$ GeV, no distinction between the regions is possible due to the inverse relationship between bend and energy for hadronic tracks.

penetration depth for hadrons compared to photons, it is not possible to draw a straight line connecting the EMCAL cluster center, PC3 hit and collision vertex for charged hadrons that travel through (and bend in) the magnetic field. Thus there will be some energy-dependent θ_{CV} region associated with these particles which can be used to exclude them from the analysis.

- (3) Large θ_{CV} : The phase space for combinatorial association of an EMCAL cluster with an unrelated PC3 hit increases linearly with $\tan(\theta_{CV})$. Thus random association dominates this region and we should not throw out these clusters.

After applying all other cluster cuts, each reconstructed pair invariant mass was assigned to the (energy, θ_{CV}) bin of both of its clusters, and a θ_{CV} interval was chosen as a function of cluster energy such that the exclusion of clusters in this interval minimized the statistical uncertainty on $A_{LL}^{x^0}$ after background A_{LL} subtraction. The resulting θ_{CV} intervals are shown in Fig. 4 for clusters in the PbSc with energies below 1.9 GeV, above which the deflection of charged hadrons in the magnetic field becomes too small to make a clear separation in θ_{CV} . Due to the decreased response of the PbGL to hadrons, no additional benefit for the charge veto cut on top of the other cuts was found and the charge veto cut was not applied. In contrast, when selecting on PbSc clusters with energy < 1.9 GeV, the charge veto cut improved the statistical uncertainty on $A_{LL}^{x^0}$ in the 1–1.5 GeV/ c p_T bin by 5% when applied on top of

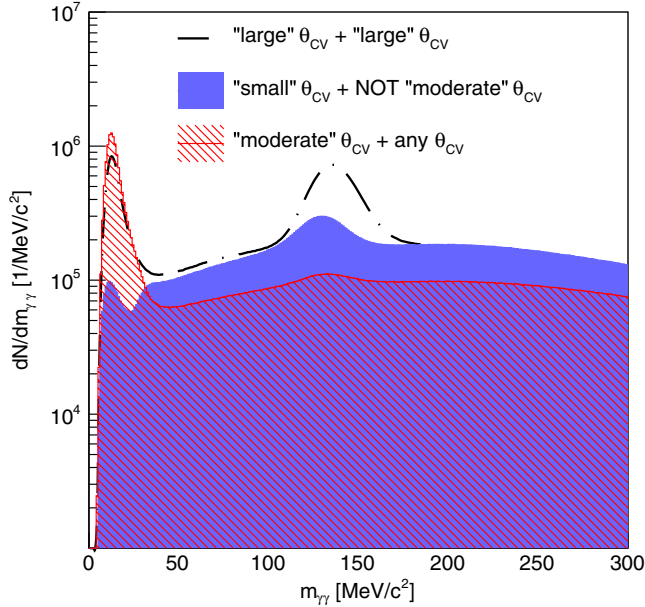


FIG. 5 (color online). Yield of cluster pairs in the PbSc with p_T of 1–1.5 GeV/c for different θ_{CV} requirements as a function of invariant mass (calculated assuming both clusters are photons), in the PbSc only and for $E_{\text{cluster}} < 1.9$ GeV. The ratio of the “small” + “not moderate” to the “large” + “large” yield in the π^0 mass-peak region is consistent with the material budget of $\approx 10\%$ fractional radiation length in the magnetic-field region before the PC3.

all other cluster cuts. The improvement in the 1.5–2 GeV/c p_T bin was 3%, and less than 1% in bins thereafter.

The invariant mass distribution near the π^0 mass peak reconstructed using clusters in the PbSc is shown in Fig. 5 for different θ_{CV} requirements. It is clear that the signal to background ratio for the π^0 meson is significantly smaller for clusters with a moderate θ_{CV} , due to hadron contamination in the photon candidates. The sample with one small θ_{CV} cluster is dominated by conversions, and some energy is lost in this process, causing the π^0 mass peak to reconstruct at slightly lower mass. The effect of this mass shift was studied and found to have a negligible impact on the final asymmetries.

2. Time-of-flight cut

A particular hardware-based effect that became apparent with increases in the instantaneous luminosities delivered to the experiments in 2009 involved the readout electronics for the EMCal. When the trigger fires, the signal in each EMCal tower is compared with an analog-buffered value from 424 ns, or four crossings, earlier. Due to the long decay time of an EMCal signal, any energy deposit occurring in the three previous crossings is read out. Pileup is negligible due to the fine lateral segmentation of the EMCal, so only the combinatorial background is affected. In the 2009 run, the likelihood for a collision in at least one of three previous

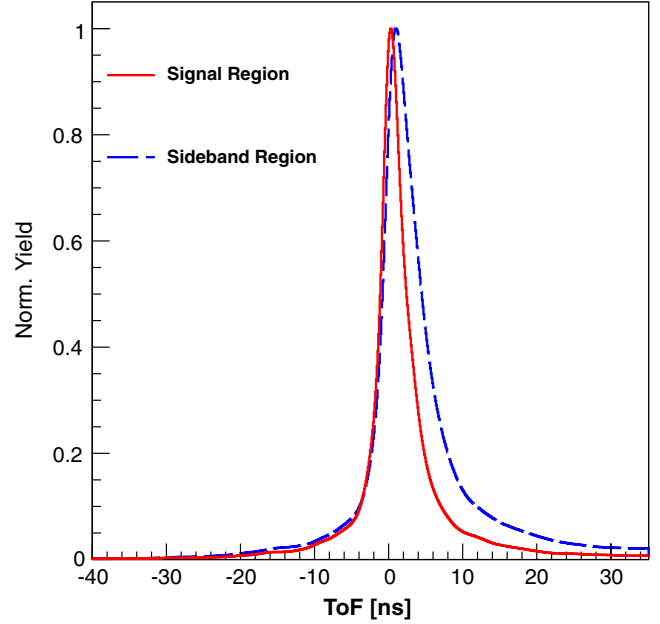


FIG. 6 (color online). Normalized ToF distributions for the lower energy cluster in cluster pairs passing all cuts except the ToF cut. The distributions are plotted for pairs with invariant mass reconstructions in the π^0 signal or sideband regions defined in the text.

crossings was significant at about 22%. One cut in particular that can reduce this effect is the ToF cut.

The ToF for a given EMCal cluster is given relative to t_0 , the initial time of the collision as measured by the BBC. Scatter in t_0 widens the ToF distribution from the nominal 0.7 ns resolution. The resulting distributions are shown in Fig. 6 for clusters contributing to the π^0 signal and sideband regions of the invariant mass spectrum. Photon candidates in this analysis are required to reach the EMCal within $^{+8}_{-6}$ ns of the expected ToF for a photon, which removes the low energy hadrons that skew the distribution to higher ToF as well as other out of time clusters. The cut also reduces the contribution of clusters from previous crossings. Even though the circular buffering in the EMCal readout makes the ToF measurement insensitive to timing offsets that are multiples of the beam-crossing period, the fact that different crossings have independent t_0 effectively smears the ToF distribution further. This is the dominant effect in increasing the likelihood of previous-crossing clusters to have a ToF outside the cut window.

This background can be studied in more detail by analyzing specific sets of crossings that follow one- or two-bunch empty crossings and therefore contain a smaller number of previous-crossing clusters. We define the following crossing selections for study based on the number of previous crossings that can contribute clusters given a four-crossing (current plus three) memory:

- (i) +0: The three previous crossings are empty.
- (ii) +1: One of the three previous crossings is filled.

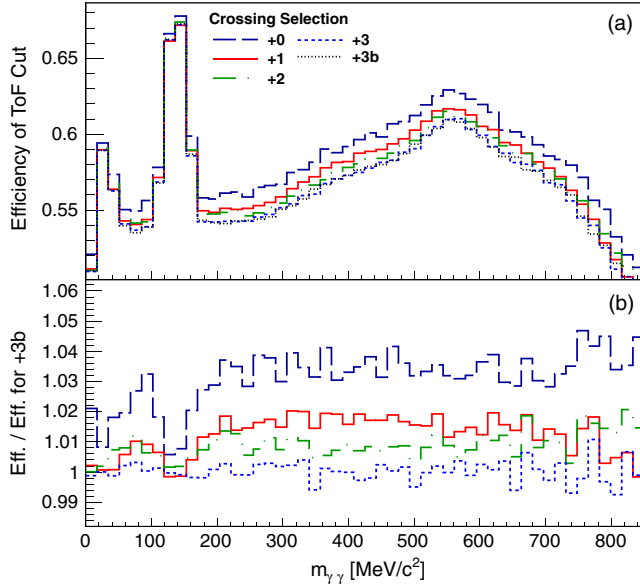


FIG. 7 (color online). (a) Efficiency of ToF cut, with the minimum energy, trigger, and off-line z -vertex cuts already applied, for different crossing selections defined in the text, and for a p_T range of 2–4 GeV/ c . The energy asymmetry cut has not been applied here, and the decreased efficiency in the η mass region is due to the larger background fraction. (b) Ratio of the histograms in (a) to the histogram with crossing selection +3b.

- (iii) +2: Two of the three previous crossings are filled.
- (iv) +3: All three previous crossings are filled.
- (v) +3b: Same as +3 but spaced further from empty crossings.

Figure 7 shows the efficiency of (fraction of events passing) the ToF cut on the various selections. The efficiency decreases as the selection moves away from the empty crossings and the previous-crossing cluster background increases, indicating that the ToF cut is more effective at removing this specific type of background than the total background. Also, from selection +0 to +3, the relative efficiency in the π^0 peak region decreases by about 0.5% compared to a decrease of roughly 3% in the high mass background efficiency. The smaller change for the peak region is due to the trigger cut (see next section) removing true mesons from previous crossings. As expected, there is no significant change in cut efficiency between selections +3 and +3b since the buffer encompasses only three previous crossings.

B. π^0 and η selection

From the photon candidates surviving the cuts discussed above, all combinatorial pairings are reconstructed using the relation for a decay into two massless photons,

$$m_{\gamma\gamma}^2 \equiv 2E_1E_2(1 - \cos \theta), \quad (4)$$

where E_1 and E_2 are the energies of the two clusters and θ is the angle between the two vectors from the decay vertex

(assumed here equal to the collision vertex, which has a negligible impact on resolution) to the EMCal clusters.

An additional cut is applied to the photon pairs to ensure that they triggered the event, so as to not introduce a bias towards higher multiplicity events or convolute the π^0 - or η -meson asymmetry with that of a different trigger particle. All trigger tiles overlapping a 12×12 tower region ($\Delta\eta \sim 0.1$, $\Delta\phi \sim 0.1$ rad) are read out as one “supermodule,” which is the smallest segmentation in the recorded trigger information. We require that the central tower of the higher energy photon candidate cluster be located within a supermodule firing the trigger. This also effectively guarantees that the cluster comes from the current, and not a previous, crossing.

To further reduce the background for the η , an energy asymmetry cut is applied to exclude cluster pairs, where

$$\frac{|E_1 - E_2|}{E_1 + E_2} \geq a. \quad (5)$$

For the η analysis, a value $a = 0.7$ was used, which optimized the uncertainty on A_{LL}^{η} . The application of this cut in addition to all other cluster and pair cuts improved the uncertainty by about 50% in the 2–3 GeV/ c p_T bin and about 7% in the 3–4 GeV/ c bin. For the $A_{LL}^{\pi^0}$ analysis, the energy asymmetry cut was not used, since its application results in a large uncertainty *increase* in each p_T bin, owing to the fact that the effect of the energy asymmetry cut on signal and background is comparable and the signal to background ratio is much higher for the π^0 meson.

The final invariant mass spectra with all cuts applied are shown separately for the π^0 and η mesons for a single p_T bin in Fig. 8. The signal (solid red) and sideband (hatched blue) regions used in the A_{LL} analyses are illustrated for each meson.

C. Asymmetry analysis

Experimentally, measuring A_{LL} as written in Eq. (2) is not feasible due to the sizable systematic uncertainties in any cross section measurement, and the small asymmetries expected. Therefore, A_{LL} is expressed as

$$A_{LL} = \frac{1}{P_B P_Y} \frac{N_{++} - RN_{+-}}{N_{++} + RN_{+-}}, \quad (6)$$

where N is the observable meson yield in the given helicity state and $P_{B(Y)}$ is the polarization of the blue (yellow) beam. R is the relative luminosity between helicity states, and is defined as

$$R = \frac{L_{++}}{L_{+-}}, \quad (7)$$

where L is the luminosity sampled in each helicity state.

By writing A_{LL} in this way, we are implicitly assuming that all acceptance and efficiency corrections are helicity

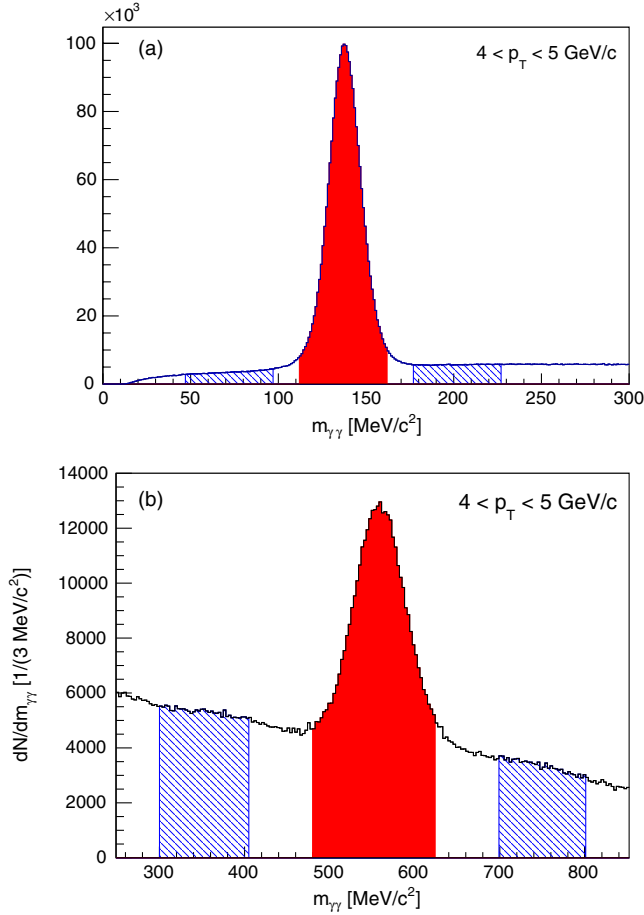


FIG. 8 (color online). (a) Two-photon invariant mass in the region of the π^0 mass for the $4 < p_T < 5$ GeV/ c bin with all cuts except the energy asymmetry cut applied, as discussed in the text. (b) Two-photon invariant mass in the region of the η mass with all cuts including the energy asymmetry cut applied, as discussed in the text. In both plots, the red solid region shows the signal region and the blue hatched region shows the background sidebands used in the asymmetry analysis.

and crossing independent. The detector acceptance and reconstruction efficiencies do not change on the scale of hundreds of nanoseconds, which is the typical time between helicity flips in RHIC, so these are not an issue. In the case of the trigger efficiency, however, this assumption does not hold due to the design of the trigger circuit. As discussed in Sec. II B, the even and odd crossings have different trigger circuits with different effective trigger thresholds. Therefore, the analysis is done separately for odd and even crossings for $p_T < 7$ GeV/ c . Above this p_T , the triggers are maximally efficient and there is no observed dependence on the trigger circuit.

Similarly, for R , we do not measure the ratio of luminosities recorded in each helicity state, but instead the ratio of MB triggered events, again assuming that efficiency and acceptance cancel in the ratio. The accuracy of this assumption, as well as the assumption that the MB

trigger has no inherent asymmetry, are discussed below. The latter leads to the largest systematic uncertainty in the determination of A_{LL} .

As seen in Fig. 8, the two-photon mass yield in the π^0 or η mass-peak region (solid red shading) comprises both signal and background. The asymmetry measured in this region, A_{LL}^{S+B} , mixes both the signal asymmetry, A_{LL}^S , and the asymmetry in the background component, A_{LL}^B . The relationship between these three asymmetries in the mass peak region can be written as

$$A_{LL}^S = \frac{A_{LL}^{S+B} - w_{BG} A_{LL}^B}{1 - w_{BG}},$$

$$\Delta A_{LL}^S = \frac{\sqrt{(\Delta A_{LL}^{S+B})^2 + r^2 (\Delta A_{LL}^B)^2}}{1 - w_{BG}}, \quad (8)$$

where w_{BG} is the background fraction in the peak region. For the π^0 meson, we define the peak region as $112 < m_{\gamma\gamma} < 162$ MeV/ c^2 , which corresponds to roughly 2σ about the mean of the mass peak at low p_T . Similarly, for the η meson, the peak region is defined as $480 < m_{\gamma\gamma} < 620$ MeV/ c^2 . The peak positions do not correspond exactly to the known mass values for the mesons due to energy smearing effects in the EMCal.

The background fraction w_{BG} is extracted from a fit to the mass range near the meson mass peak: 50–300 MeV/ c^2 for the π^0 meson, and 300–800 MeV/ c^2 for the η meson. In both cases, the fit function comprises a Gaussian to describe the mass peak plus a third-order polynomial to describe the background. w_{BG} is defined as the integral of the background polynomial in the mass peak range $[m_1, m_2]$ divided by the total yield in this same range:

$$w_{BG} = \frac{\int_{m_1}^{m_2} dm (a_0 + a_1 m + a_2 m^2 + a_3 m^3) / \text{bin width}}{\text{Yield}_{[m_1, m_2]}}. \quad (9)$$

Variations of the initial fit parameters, range, and histogram binning showed no significant modification to w_{BG} except in the 12–15 GeV/ c p_T bin, where modifying the binning led to a 2.1% change in $A_{LL}^{\pi^0} / \sigma_{A_{LL}^{\pi^0}}$, attributable to the difficulty in fitting the low-statistics background in this p_T range. Average background fractions for the different p_T bins are listed in Table I.

The background asymmetry in the peak region cannot be directly measured, but if the background asymmetry is constant as a function of $m_{\gamma\gamma}$, then a measurement in the sideband regions on either side of the peak can be used instead. Figure 9 shows the asymmetry as a function of mass in the background region near the π^0 peak for several p_T bins. No indication of a mass dependence in the background asymmetry is seen. However, as discussed below, a small systematic uncertainty is evaluated for $A_{LL}^{\pi^0}$ to account for any mass dependence. In the case of A_{LL}^{η} , any

TABLE I. Average background fractions under the π^0 and η peaks, $w_{\text{BG}}^{\pi^0}$ and w_{BG}^{η} , in each p_T bin for the 2009 data. In the actual analysis, separate calculations of w_{BG} were used in different data subsets (e.g., even and odd crossings).

$p_T^{\pi^0}$ bin (GeV/c)	$w_{\text{BG}}^{\pi^0}$ (%)	p_T^{η} bin (GeV/c)	w_{BG}^{η} (%)
1–1.5	49		
1.5–2	34		
2–2.5	23	2–3	78
2.5–3	17		
3–3.5	13	3–4	57
3.5–4	12		
4–5	11	4–5	46
5–6	11	5–6	43
6–7	10	6–7	43
7–9	10	7–9	39
9–12	9.1		
12–15	5.5		

background dependence is negligible when considering the limited statistics. To increase statistics, the yields in the sidebands on both sides of the peak region are summed to calculate the background asymmetry. The sideband regions are shown in Fig. 8, and for the π^0 meson are defined as $47 < m_{\gamma\gamma} < 97 \text{ MeV}/c^2$ and $177 < m_{\gamma\gamma} < 227 \text{ MeV}/c^2$. For the η meson, they are $300 < m_{\gamma\gamma} < 400 \text{ MeV}/c^2$ and $700 < m_{\gamma\gamma} < 800 \text{ MeV}/c^2$.

As written in Eq. (6), A_{LL} is calculated for peak and background sidebands in each RHIC fill. Due to the

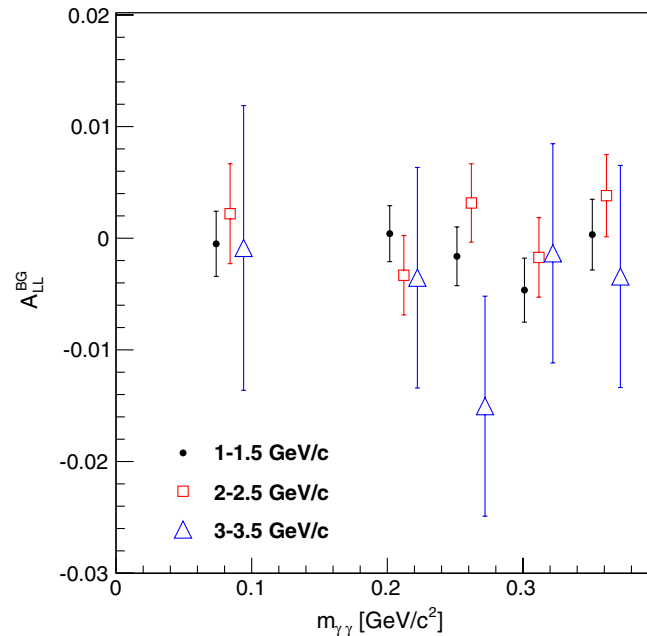


FIG. 9 (color online). A_{LL} vs $m_{\gamma\gamma}$ for the background region near the π^0 mass peak for three p_T bins: 1–1.5 GeV/c (black circle), 2–2.5 GeV/c (red square) and 3–3.5 GeV/c (blue triangle), for a single spin pattern in odd crossings. The peak region A_{LL} is not shown. No $m_{\gamma\gamma}$ dependence is found.

variation in trigger electronics discussed above, the analysis is done separately for even and odd crossings. For each of the four spin patterns, A_{LL}^S in even or odd crossings is calculated using Eq. (8) with the statistically weighted average over fills of A_{LL}^{S+B} and A_{LL}^B . The eight results (four spin patterns for even crossings and four spin patterns for odd crossings) are found to be consistent and combined to arrive at the final A_{LL}^S .

D. Systematic uncertainties

In this section we discuss the systematic uncertainties relevant to the π^0 and η analyses, chief among them the uncertainty in the determination of relative luminosity. The various contributions are summarized in Table II.

1. Relative luminosity

To account for luminosity differences between same (++) and opposite (+−) helicity crossings, we include a factor R for relative luminosity normalization in Eq. (7). Unlike in lepton-proton scattering experiments, where QED calculations are precise enough to control for spin asymmetries in the extraction of relative luminosity from the inclusive DIS cross section, there is no suitable process in $\bar{p} + \bar{p}$ that is both high rate and precisely calculable. For absolute luminosity in cross section measurements, we use a machine luminosity calculated from beam currents and beam spatial profiles, the latter of which are extracted via an experimental technique called a Vernier Scan [22]. The resulting uncertainty on this machine luminosity is too large for use in asymmetry calculations. However, accurate measurements of R can be made using any detector insensitive to physics asymmetries.

For our purposes, we use the ratio of two-arm coincidence BBC MB triggers with a reconstructed vertex $|z| < 30 \text{ cm}$ as R :

$$R = \frac{N_{++}^{\text{BBC}}}{N_{+-}^{\text{BBC}}}. \quad (10)$$

TABLE II. Summary of systematic uncertainties on π^0 and η A_{LL} for the 2009 data. The systematics listed as “ π^0 only” were not evaluated for the η asymmetries.

Description	$\Delta A_{LL}(\text{syst})$	p_T correlated?	Note
Relative luminosity	1.4×10^{-3}	Yes	...
Polarization magnitude	$0.065 \times A_{LL}$	Yes	...
Polarization direction	$^{+0.026}_{-0.042} \times A_{LL}$	Yes	...
w_{BG} Determination	$< 0.01 \times \Delta A_{LL}^{\text{stat}}$	No	π^0 only
EMCal readout	1.6×10^{-4}	No	π^0 only, lowest p_T bin

However, we should be careful that this R is not biased by sensitivity of the BBC to some unmeasured physics asymmetry. To test for sensitivity of the BBC to a double helicity asymmetry, we compare to two-arm coincidence ZDC triggered events (also with a reconstructed vertex $|z| < 30$ cm) via

$$A_{LL}^R \equiv \frac{1}{P_B P_Y} \frac{r_{++} - r_{+-}}{r_{++} + r_{+-}},$$

$$r \equiv \frac{N_{ZDC}}{N_{BBC}}. \quad (11)$$

We take the resulting asymmetry *plus* its statistical uncertainty as a systematic uncertainty on our knowledge of the double helicity asymmetry of BBC triggered events. We choose the ZDC for comparison because, in addition to having a different geometrical acceptance (see Sec. II B), it samples a significantly different class of events than the BBC. The BBC fires predominantly on charged particles and is dominated by low- p_T soft physics, whereas the ZDC samples mainly diffractive physics and, due to its location behind the accelerator's bending magnets, which sweep away most charged particles, fires on neutrons, photons, and hadronic showers from scattered protons interacting with the machine elements. The asymmetries in the different physics sampled by the ZDC and the BBC cannot be directly calculated. However, comparing these two detectors with different physics sensitivities increases the likelihood that any nonzero asymmetries would be apparent.

Table III lists the measured asymmetries for three years of longitudinally polarized $\vec{p} + \vec{p}$ running at RHIC. For each measurement, a crossing-to-crossing correction for smearing due to the ~ 30 cm online position resolution of the ZDC was applied but found to have little effect on the central A_{LL}^R value or its total uncertainty. Given that A_{LL}^R is significantly higher for the present (2009) data, an additional cross-check was performed there, motivated by the increased instantaneous luminosity delivered in 2009: the calculation of A_{LL}^R using an alternate definition for the luminosities sampled by the BBC and ZDC. The issue is that for any simple trigger that returns only one bit of information (yes or no), the ratio of triggered events to total

TABLE III. Measured value of A_{LL}^R in $\sqrt{s} = 200$ GeV $\vec{p} + \vec{p}$ running in the given years. A_{LL}^R *plus* its uncertainty is used as the total shift uncertainty for any physics asymmetry result using the BBC as a relative luminosity monitor. The run-year-correlated part of the uncertainty is taken to equal the maximal overlap in A_{LL}^R across years: 0.42×10^{-3} . The remaining part of each year's A_{LL}^R *plus* its statistical uncertainty is taken as a run-year uncorrelated part.

Data Year	$A_{LL}^R \times 10^{-3}$	$\Delta A_{LL}^R (\text{stat} + \text{syst}) \times 10^{-3}$
2005	0.42	0.23
2006	0.49	0.25
2009	1.18	0.21

$\vec{p} + \vec{p}$ collisions tends to decrease with rate as multiple collisions in a single crossing become more common. For the BBC, which, accounting for acceptance and efficiency, has a $55\% \pm 5\%$ chance to detect a single inelastic $p + p$ collision, this was the dominant effect in the 2009 run. The ZDC has a much lower efficiency, and here the dominant rate effect was instead the increased likelihood of coincidence for unrelated background events in the two arms, which lead to an increased overcounting of the $\vec{p} + \vec{p}$ collisions. Using a set of scaler boards that were under commissioning during (and thus not available over the entirety of) the 2009 run, correlations between hits in the two arms were counted in each crossing and used to calculate the quantity

$$\epsilon_N \epsilon_S \lambda = \ln \left(1 - \frac{N_{\text{OR}}}{N_{\text{clock}}} \right) - \ln \left(1 - \frac{N_S}{N_{\text{clock}}} \right) - \ln \left(1 - \frac{N_N}{N_{\text{clock}}} \right), \quad (12)$$

where $N_N(S)$ is the trigger count in the North (South) arm and N_{OR} is the count of triggers in the North, South, or both arms. All are normalized to the number of beam crossings N_{clock} . λ is the average number of events per bunch intersection capable of triggering both arms of the detector, and ϵ_N, ϵ_S are factors for the efficiency \times acceptance of the arms for these events [36]. Because the z vertex cannot be reconstructed if only one arm is triggered, this quantity necessarily covers the entire z -vertex range (the typical collision distribution in 2009 running had width $\sigma_z \approx 45$ cm). The advantages of this are that it does not undercount multiple collisions, and events that are not capable of triggering both arms of the detector (such as noise or single-diffractive collisions) are removed

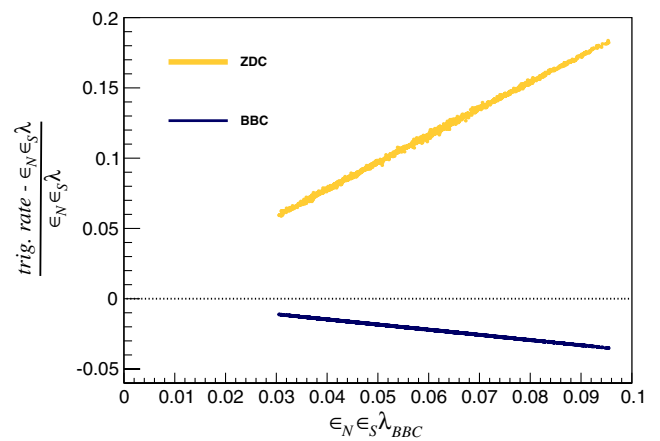


FIG. 10 (color online). Relative difference between the measured trigger rate and the quantity in Eq. (12) plotted for all beam crossings in a fraction of the present data set.

analytically. The relative difference between $\epsilon_N \epsilon_S \lambda$ and trigger rate for the two detectors is shown in Fig. 10.

The resulting values $\epsilon_N \epsilon_S \lambda$ for the BBC and ZDC were used in Eq. (11) with

$$r \equiv \frac{\epsilon_N \epsilon_S \lambda_{ZDC}}{\epsilon_N \epsilon_S \lambda_{BBC}}, \quad (13)$$

and the resulting A_{LL}^R was consistent with using the coincidence determination in Eq. (11), and thus the increased A_{LL}^R in 2009 over previous years could not be attributed to increases in instantaneous luminosity. The coincidence determination yielded the quoted systematic uncertainty,

$$A_{LL}^R + \delta A_{LL}^R = 1.2 + 0.2 \times 10^{-3} = 1.4 \times 10^{-3}, \quad (14)$$

which is fully correlated across p_T and between the π^0 and η results.

2. Background fraction determination

Another source of systematic uncertainty arises from the extraction of background fractions for the π^0 and η mass peak regions directly from the data. In particular, the background fraction under the peak regions is calculated from the result of an empirical fit to the diphoton invariant mass spectrum as in Eq. (9).

Since the overall normalization is not fixed in the fit and the Gaussian part is not used in the calculation, the determination of w_{BG} is not particularly sensitive to the shape assumption for the π^0 mass peak. Still, to check for any systematic effect, the π^0 analysis was rerun with the bin width doubled in all invariant mass histograms, which has more impact on the resolution of the sharp peak than the relatively flat background. The final $A_{LL}^{\pi^0}$ results changed by less than 1% of the statistical uncertainty in all but the 12–15 GeV/ c p_T bin, where the change was 2.1%.

3. Event overlap in EMCal readout

As discussed above in Sec. III A, readout of the EMCal includes clusters from any of the three previous crossings. The trigger requirement ensures that one photon of each pair is in the correct crossing, which ensures that true π^0 and η mesons are reconstructed from the correct crossing. However, the combinatorial background may mix clusters from previous crossings (with a different helicity combination) with clusters from the correct crossing. The yield of this helicity-mixed background depends on the luminosity of previous crossings, and differs significantly for crossings following empty crossings.

To test for any impact of this effect on the background asymmetry, A_{LL} was calculated with a reduced set of cuts using Eq. (8) for the four different spin patterns in RHIC. Differences were seen in the background asymmetries for the different spin patterns, particularly at low p_T . An $m_{\gamma\gamma}$ dependence in the spin pattern dependent asymmetries was

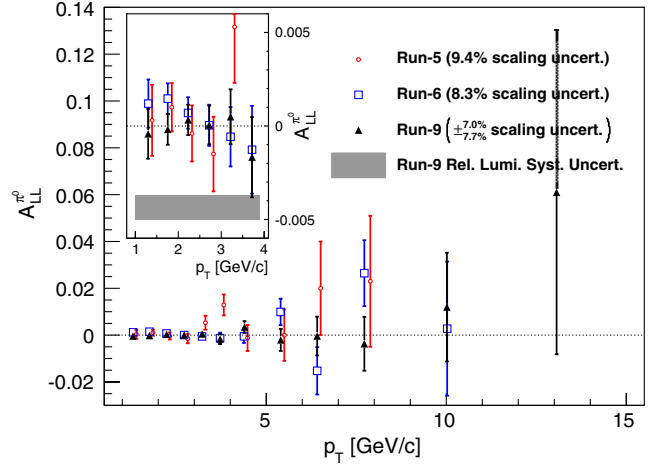


FIG. 11 (color online). A_{LL} vs p_T for π^0 mesons for the 2005 (red circle), 2006 (blue square) and 2009 (black triangle) PHENIX data sets. The 2009 relative luminosity systematic uncertainty is shown only in the inset, but it applies across the entire p_T range.

also visible. These effects were mitigated by the full set of cluster cuts, including the ToF cut described in Sec. III A 2, which is more effective than the other cuts in targeting previous-crossing background. Additionally, the asymmetries in the two sidebands and across higher mass regions were compared to estimate a possible systematic uncertainty arising from any remaining effect. For the π^0 analysis, the systematic uncertainty in the 1.0–1.5 GeV/ c bin was 1.6×10^{-4} , and for all higher p_T bins the uncertainty was less than 10^{-4} , which is negligible compared to the relative luminosity systematic uncertainty as well as the statistical uncertainty.

In addition, to avoid the pooling of data with different nonzero background asymmetries, data from the four possible spin patterns were analyzed separately through the background subtraction step [Eq. (8)], except for in the

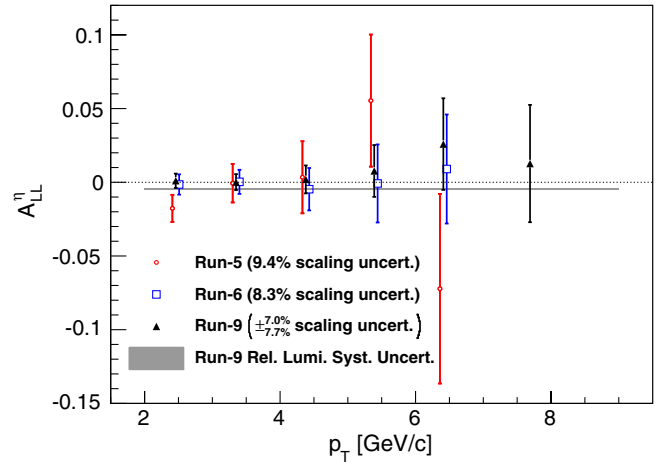


FIG. 12 (color online). A_{LL} vs p_T for η mesons for the 2005 (red circle), 2006 (blue square) and 2009 (black triangle) PHENIX data sets.

TABLE IV. $\pi^0 A_{LL}$ measurements at $\sqrt{s} = 200$ GeV from the 2005, 2006, and 2009 RHIC runs, along with statistical uncertainties. The systematic uncertainties for the three years are: relative luminosity (shift uncertainty): 6.5×10^{-4} , 7.5×10^{-4} , and 14.0×10^{-4} polarization (scale uncertainty): 9.4%, 8.3%, and $^{+7.0\%}_{-7.7\%}$.

$p_T^{\pi^0}$ bin (GeV/c)	2005				2006			2009		
	$\langle p_T^{\pi^0} \rangle$ (GeV/c)	$A_{LL}^{\pi^0} \times 10^{-3}$	$\Delta A_{LL}^{\pi^0} \times 10^{-3}$	$\langle p_T^{\pi^0} \rangle$ (GeV/c)	$A_{LL}^{\pi^0} \times 10^{-3}$	$\Delta A_{LL}^{\pi^0} \times 10^{-3}$	$\langle p_T^{\pi^0} \rangle$ (GeV/c)	$A_{LL}^{\pi^0} \times 10^{-3}$	$\Delta A_{LL}^{\pi^0} \times 10^{-3}$	
1–1.5	1.29	0.3	1.9	1.30	1.2	1.3	1.30	−0.4	1.3	
1.5–2	1.75	1.0	1.3	1.75	1.46	0.82	1.75	−0.19	0.82	
2–2.5	2.22	−0.4	1.5	2.23	0.70	0.84	2.23	0.33	0.81	
2.5–3	2.72	−1.5	2.0	2.72	0.0	1.1	2.72	0.1	1.0	
3–3.5	3.21	5.3	3.0	3.22	−0.6	1.6	3.22	0.5	1.5	
3.5–4	3.72	12.9	4.5	3.72	−1.3	2.3	3.72	−1.7	2.2	
4–5	4.38	−1.2	5.6	4.38	−0.5	2.9	4.40	3.5	2.5	
5–6	5.40	0	11	5.40	9.9	5.7	5.40	−2.1	4.7	
6–7	6.41	20	20	6.41	−15	10	6.41	−0.4	8.3	
7–9	7.79	23	28	7.74	26	14	7.72	−4	12	
9–12	N/A	N/A	N/A	10.0	3	29	10.0	12	23	
12–15	N/A	N/A	N/A	N/A	N/A	N/A	13.1	61	69	

π^0 9–12 and 12–15 GeV/c p_T bins where, to increase statistics, patterns equivalent for a double-helicity asymmetry (i.e. with “same” and “opposite” helicity crossings unchanged) were combined.

4. Polarization direction

Another hardware based uncertainty that has been present in all longitudinal RHIC runs is that of the remaining transverse polarization component after the beams have passed through the spin rotator magnets, discussed in detail in Sec. II A. The total resultant scaling uncertainty in the longitudinal component of $P_B P_Y$, which applies globally to the 2009 data set, is $((^{+0.026}_{-0.042})$. This can be added in quadrature to the polarization scale uncertainty listed in Sec. II A, and the results of that combination are given in Figs. 11 and 12 as well as Tables IV and V.

5. Searches for additional systematic uncertainty sources

To test for additional RHIC fill-to-fill uncorrelated systematic uncertainties that may have been overlooked, we applied a statistical bootstrapping technique to the data.

For each of ten-thousand iterations, a separate random spin pattern was chosen for each fill, and all quantities were calculated according to this pattern. This allowed us to produce, for the various “peak” and “sideband” regions, simulated distributions for A_{LL} , δA_{LL} , and χ^2 from a fit of A_{LL} across RHIC fills. The result of this test was that the uncertainties were being underestimated above $p_T \approx 7$ GeV/c for the sideband region and overestimated at low p_T for both regions. The sideband region underestimation was traced to low background statistics at high p_T resulting in the violation of Gaussian distribution assumptions for error propagation. Since the background fraction w_{BG} is small at high p_T , this effect is negligible in the final result. The overestimation of uncertainties at low p_T is due to conservative calculation of uncertainties in the cases where triggers were scaled to match the data acquisition bandwidth. For the π^0 , the largest overestimation was about 6% of the statistical uncertainty, for the signal region in the lowest p_T bin.

Measurements of single-spin asymmetries, in which the polarization of one beam is summed over, were also performed. Such asymmetries, if physical, would be parity

TABLE V. ηA_{LL} measurements at $\sqrt{s} = 200$ GeV from the 2005, 2006, and 2009 RHIC runs, along with statistical uncertainties. The systematic uncertainties for the three years are: relative luminosity (shift uncertainty): 6.5×10^{-4} , 7.5×10^{-4} , and 14.0×10^{-4} and polarization (scale uncertainty): 9.4%, 8.3%, and $^{+7.0\%}_{-7.7\%}$.

p_T^η bin (GeV/c)	2005				2006			2009		
	$\langle p_T^\eta \rangle$ (GeV/c)	$A_{LL}^\eta \times 10^{-3}$	$\Delta A_{LL}^\eta \times 10^{-3}$	$\langle p_T^\eta \rangle$ (GeV/c)	$A_{LL}^\eta \times 10^{-3}$	$\Delta A_{LL}^\eta \times 10^{-3}$	$\langle p_T^\eta \rangle$ (GeV/c)	$A_{LL}^\eta \times 10^{-3}$	$\Delta A_{LL}^\eta \times 10^{-3}$	
2–3	2.41	−17.7	9.2	2.51	−1.5	6.9	2.46	1.1	4.9	
3–4	3.30	−1	13	3.40	0.3	8.2	3.35	0.1	5.4	
4–5	4.33	3	24	4.43	−5	14	4.38	2.0	9.5	
5–6	5.34	55	45	5.44	−1	27	5.39	8	18	
6–7	6.36	−72	64	6.46	9	37	6.41	26	31	
7–9	N/A	N/A	N/A	N/A	N/A	N/A	7.69	13	40	

TABLE VI. Combined $\pi^0 A_{LL}$ values from the PHENIX data sets at $\sqrt{s} = 200$ GeV. Fully p_T correlated systematic uncertainties that are considered uncorrelated by run year are given in the table and are shown for the two main sources of systematic uncertainties: relative luminosity (RL) and polarization (P).

$p_T^{\pi^0}$ bin (GeV/c)	$\langle p_T^{\pi^0} \rangle$ (GeV/c)	$A_{LL}^{\pi^0} \times 10^{-4}$	$\Delta A_{LL}^{\pi^0}$ (stat) $\times 10^{-4}$	$\Delta A_{LL}^{\pi^0}$ (RL syst) $\times 10^{-4}$	$\Delta A_{LL}^{\pi^0}$ (P syst) $\times A_{LL}^{\pi^0}$	$\Delta A_{LL}^{\pi^0}$ (total syst) $\times 10^{-4}$
1–1.5	1.30	5.1	8.5	3.5	3.4%	3.6
1.5–2	1.75	9.6	5.5	3.3	3.5%	3.3
2–2.5	2.23	3.9	5.8	3.4	3.5%	3.4
2.5–3	2.72	−2.3	7.4	3.6	3.4%	3.7
3–3.5	3.22	6	11	4.0	3.2%	4.0
3.5–4	3.72	2	15	4.1	3.1%	4.1
4–5	4.39	13	18	4.3	3.1%	4.3
5–6	5.40	26	35	4.5	3.0%	4.5
6–7	6.41	−39	61	4.5	2.9%	4.6
7–9	7.74	96	85	4.5	2.9%	5.3
9–12	10.0	80	180	5.8	3.3%	6.5
12–15	13.1	610	690	10	3.0%	21

TABLE VII. Combined ηA_{LL} values from the PHENIX data sets at $\sqrt{s} = 200$ GeV. Fully p_T correlated systematic uncertainties that are considered uncorrelated by run year are given in the table and are shown for the two main sources of systematic uncertainties: relative luminosity (RL) and polarization (P). The run-year correlated parts of the polarization scale uncertainty, 4.8%, and the relative luminosity shift uncertainty, 4.2×10^{-4} , are not included.

p_T^η bin (GeV/c)	$\langle p_T^\eta \rangle$ (GeV/c)	$A_{LL}^\eta \times 10^{-4}$	ΔA_{LL}^η (stat) $\times 10^{-4}$	ΔA_{LL}^η (RL syst) $\times 10^{-4}$	ΔA_{LL}^η (P syst) $\times A_{LL}^\eta$	ΔA_{LL}^η (total syst) $\times 10^{-4}$
2–3	2.46	−27	37	4.5	3.0%	4.6
3–4	3.35	1	44	4.7	2.8%	4.7
4–5	4.38	2	77	4.8	2.8%	4.8
5–6	5.39	100	140	4.8	2.8%	5.5
6–7	6.41	80	230	4.4	3.0%	5.0
7–9	7.69	130	410	10	3.0%	11

violating. As expected for a parity-conserving QCD process, they were found to be consistent with zero. Comparisons were also made between the two different electromagnetic calorimeter technologies. In these comparisons, both double and single-spin asymmetries were measured separately in the PbSc and PbGl, and no inconsistency between the two detectors was found.

IV. RESULTS

The π^0 and ηA_{LL} values as a function of p_T for the 2009 data set are shown in Figs. 11 and 12, respectively, and given in Tables IV–VII. The results are compared with previously published results from 2005 and 2006 [16,20], with which they are consistent. The relative luminosity systematic uncertainty for the 2009 data set is shown only in the inset of Fig. 11 but applies to all of the points. The polarization uncertainties discussed above are not shown on the data points but are listed in the legend. The results are consistent in all cases.

V. DISCUSSION

In Figs. 13 and 14, the 2005, 2006 and 2009 results have been combined for the π^0 and η , respectively, with the

uncorrelated part of the systematic uncertainties combined and shown on the points. The year-to-year correlated parts of the polarization and relative luminosity uncertainties are given in the legend.

Both the η and π^0 asymmetries are consistent with the best fit of a global analysis of DIS data that allows at the input scale only quark contributions to A_{LL} : the GRSV-zero scenario, which assumes $\Delta g(x, \mu^2) = 0$ at an NLO input scale $\mu^2 = 0.40$ GeV² [37]. This consistency can be quantified relative to the related GRSV-std scenario, in which the gluon polarization is not fixed (nor is it well constrained). The difference between these two scenarios in a statistical-uncertainty-only comparison to the combined π^0 data in the 2–9 GeV/c p_T range is $(\Delta\chi^2)_{\text{GRSV}}/\text{N.D.F.} \equiv ((\chi^2)_{\text{GRSV-std}} - (\chi^2)_{\text{GRSV-zero}})/\text{N.D.F.} = 18.9/8$, a 4.3-sigma change. If all of the points are increased by the total systematic uncertainty to move them closer to the GRSV-std curve, the change is 3.3/8 or 1.8 sigma, indicating that the PHENIX π^0 data still prefer the GRSV-zero scenario. For the η asymmetries in the same p_T range, $(\Delta\chi^2)_{\text{GRSV}}/\text{N.D.F.} = 0.4/6$ or 0.6 sigma, indicating a slight preference for GRSV-zero. With the η asymmetries shifted up by the systematic uncertainty,

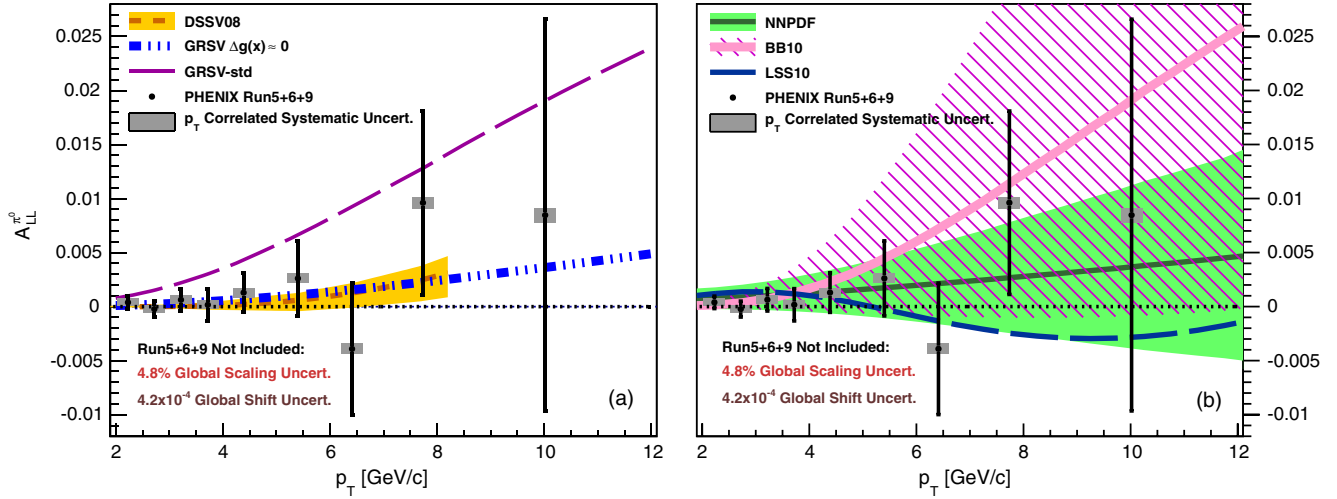


FIG. 13 (color online). Points are the combined A_{LL} vs p_T for π^0 mesons from 2005 through 2009 with the statistical uncertainty. The p_T correlated systematic uncertainty given by the gray bands is the result of combining the year-to-year uncorrelated parts of the systematic uncertainties on relative luminosity and polarization. The year-to-year correlated parts are given in the legend. Plotted for comparison are several expectations based on fits to polarized scattering data, with uncertainties where available.

there is a slight preference for GRSV-std, with $(\Delta\chi^2)_{\text{GRSV}}/\text{N.D.F.} = -0.1/6$ or 0.3 sigma.

More recent NLO global analyses of DIS-only data by Blümlein and Böttcher (BB10) [12] and Ball *et al.*

(NNPDF) [38,39], and of DIS + SIDIS data by Leader *et al.* (LSS10) [11] also allow the gluon polarization to be fit by the data, but the analyses vary in ways that affect determination of $\Delta g(x, \mu^2)$. The most significant of these differences is the BB10 assumption of a flavor-symmetric sea versus the separation of flavor-specific distributions made possible in LSS10 by the SIDIS data. This affects the gluon determination not only because of the constraint on the total polarization, but also because the analyses use functional forms for the initial pPDFs such as

$$x\Delta f_i(x, \mu^2) = N_i x^{\alpha_i} (1-x)^{\beta_i} (1 + \gamma_i \sqrt{x} + \eta_i x) \quad (15)$$

and consequentially must relate parameters between the sea and gluon distributions to enforce positivity ($|\Delta f_i(x, \mu^2)| \leq f_i(x, \mu^2)$) and to fix poorly constrained parameters.

Another issue with making a choice of functional form for $\Delta g(x, \mu^2)$ is that, even with inclusion of present $\vec{p} + \vec{p}$ data, there are no existing measurements that can test the validity of the functional form in the low- x region. For analyses like BB10 and LSS10 that do not include $\vec{p} + \vec{p}$ data, this problem extends to determination of Δg in the medium and large- x regions as well. The NNPDF analysis of DIS data avoids bias introduced in choosing a functional form for the PDFs by using neural networks to control interpolation between different x values. For example, $\Delta g(x, \mu^2)$ is parametrized as

$$\Delta g(x, \mu^2) = (1-x)^m x^{-n} NN_{\Delta g}(x), \quad (16)$$

with $NN_{\Delta g}(x)$ a neural network parametrization determined by scanning functional space for agreement with 1000 randomly distributed replicas of the experimental data. The low- and high- x terms are included for efficiency,

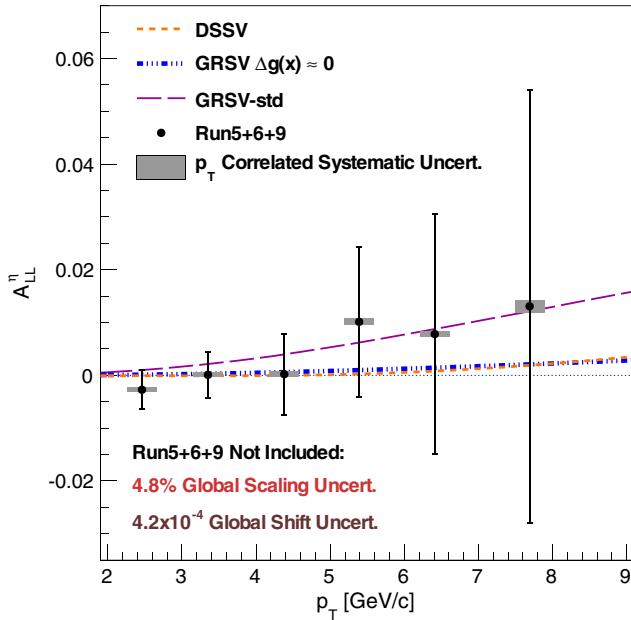


FIG. 14 (color online). Points are the combined A_{LL} vs p_T for η mesons from 2005 through 2009 with the statistical uncertainty. The p_T correlated systematic uncertainty given by the gray bands is the result of combining the year-to-year uncorrelated parts of the systematic uncertainties on relative luminosity and polarization. The year-to-year correlated parts are given in the legend. Several theoretical expectations based on fits to polarized data are also shown, which use results from [25] for the fragmentation functions.

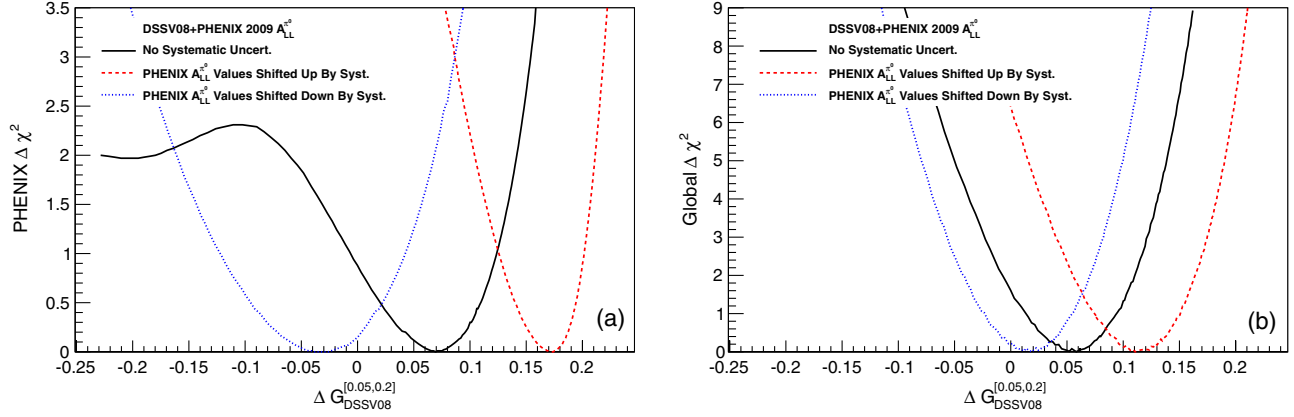


FIG. 15 (color online). Change in χ^2 as a function of $\Delta G_{\text{DSSV08}}^{[0.05,0.2]}$, when adding PHENIX 2009 π^0 data to the DSSV08 global analysis (which includes earlier PHENIX π^0 data). (a) Contribution of the combined PHENIX data at $\sqrt{s} = 200$ GeV to the global χ^2 of the DSSV08 analysis using only statistical uncertainties. The different curves show the effect of shifting only the PHENIX data points up or down by their total systematic uncertainty, which is p_T correlated. (b) The effect of shifting only the PHENIX $\sqrt{s} = 200$ GeV data points on the DSSV08 global χ^2 .

and to ensure that they do not bias the fit, m and n are chosen from a random interval for each experimental data replica such that this interval is wider than the range of effective exponents for the limiting low and high- x behavior after the neural network terms have been included.

Figure 13(b) includes $A_{LL}^{\pi^0}$ predictions based on the BB10, LSS10, and NNPDF polarized PDF determinations. For BB10 and LSS10, we evolved their published polarized PDFs to various μ^2 using the QCD-PEGASUS package [40] and used these to calculate the p_T dependent polarized cross section for inclusive π^0 production with code based on [41] that uses the DSS NLO fragmentation functions [24]. The unpolarized cross section for the denominator was calculated via the same two-step process starting from the CTEQ-6 PDFs [42]. The BB10 uncertainty band was calculated using the Hessian method with a set of polarized PDFs obtained from the parameter covariance matrix in the BB10 publication. The NNPDF prediction was provided by that group, using their polarized PDFs supplemented by preliminary W boson asymmetry measurements from the STAR experiment [43,44]. Neither the BB10 nor NNPDF prediction accounts for uncertainties in the determination of the π^0 fragmentation functions.

One feature of the predictions is that the BB10 uncertainty band is smaller than the NNPDF band at $p_T \approx 3$ GeV/ c but quickly exceeds it as p_T increases. Likewise, as can be seen in Ref. [38], at an input scale of 4 GeV², the uncertainty on the BB10 prediction for Δg , which neglects bias from the choice of functional form, is smaller than that for NNPDF at low x but exceeds it as x increases. Future inclusion of the PHENIX $A_{LL}^{\pi^0}$ into the NNPDF analysis may provide some insight into whether or not this is due to a bias in the choice of functional form at medium x , particularly in the RHIC range of [0.05,0.2].

The DSSV08 global analysis [10], which is also based on the pPDF parametrizations of Eq. (15), includes, in addition

to DIS and SIDIS data, final 2005 RHIC data [16,23] and preliminary versions of the 2006 RHIC data presented in [18,20,22]. The results of that analysis, which yields a much more accurate determination of $\Delta g(x)$, are compared with $A_{LL}^{\pi^0}$ in Fig. 13(a). We also ran an updated version of the DSSV08 analysis to include final versions of the RHIC data through 2006 [18,20,22] along with the final $A_{LL}^{\pi^0}$ results presented here. We obtained $\Delta G_{\text{DSSV08}}^{[0.05,0.2]} = 0.06_{-0.06}^{+0.04} (\Delta\chi^2 = 1)_{-0.15}^{+0.11} (\Delta\chi^2 = 9)$, where the $\Delta\chi^2 = 9$ uncertainties roughly correspond to the 2% change in $\Delta\chi^2/\chi^2_{\text{min}}$ used to determine the uncertainties in the DSSV08 global analysis. The full $\Delta\chi^2$ curve from our updated analysis is shown as the central curve in Fig. 15(b). Figure 15(a) shows the contribution from PHENIX data to that curve, and that data prefers $\Delta G_{\text{PHENIX}}^{[0.05,0.2]} = 0.07_{-0.08}^{+0.05} (\Delta\chi^2 = 1)$.

Systematic uncertainties for the RHIC data set were not included in the DSSV08 analysis. However, the PHENIX relative-luminosity systematic uncertainty now exceeds the statistical uncertainty on $A_{LL}^{\pi^0}$ in the lowest p_T bins. To understand the impact of this on the fit result, we shifted the PHENIX $\sqrt{s} = 200$ GeV data up and down by the systematic uncertainties given in the final column of Table VI, while ignoring the systematic uncertainties of all other data sets. As demonstrated in Fig. 15, this changes the global best-fit value to 0.12 or 0.02, with the value preferred by the PHENIX data changing to 0.17 or -0.03 . It is therefore necessary to include this uncertainty in future global analyses to obtain accurate determinations of ΔG .

VI. SUMMARY

We present the latest PHENIX measurements of A_{LL} in π^0 and η production in longitudinally polarized $p + p$ collisions at $\sqrt{s} = 200$ GeV. These results are compared with various existing DIS and SIDIS global analyses

[11,12,37–39] and found to be consistent within the fit uncertainties. We also find consistency with the DSSV08 global analysis [9,10], which includes versions of earlier PHENIX measurements. Addition of our new results to that analysis (as well as the updating of previous RHIC data [18,20,22]) yields a statistical-uncertainty only constraint of $\Delta G_{\text{DSSV08}}^{[0.05,0.2]} = 0.06_{-0.15}^{+0.11}$ with uncertainties determined at $\Delta\chi^2 = 9$. However, we emphasize the importance of including the relative-luminosity systematic uncertainty in future analyses that use RHIC asymmetries, since shifting the $\sqrt{s} = 200$ GeV PHENIX data alone down and up by its systematic uncertainty changes the global best-fit value $\Delta G_{\text{DSSV08}}^{[0.05,0.2]}$ from 0.02 to 0.12. A significant effort by the RHIC experiments to understand and correct for the relative-luminosity systematic effect is also currently underway. Furthermore, for the η asymmetries to be used, better determination of η fragmentation functions is needed, perhaps using the well-determined π^0 to η cross-section ratio [17,26].

ACKNOWLEDGMENTS

We thank the staff of the Collider-Accelerator and Physics Departments at Brookhaven National Laboratory and the staff of the other PHENIX participating institutions for their vital contributions. We acknowledge support from the Office of Nuclear Physics in the Office of Science of the Department of Energy, the National Science Foundation,

Abilene Christian University Research Council, Research Foundation of SUNY, and Dean of the College of Arts and Sciences, Vanderbilt University (U.S.A.), Ministry of Education, Culture, Sports, Science, and Technology and the Japan Society for the Promotion of Science (Japan), Conselho Nacional de Desenvolvimento Científico e Tecnológico and Fundação de Amparo à Pesquisa do Estado de São Paulo (Brazil), Natural Science Foundation of China (People's Republic of China), Ministry of Education, Youth and Sports (Czech Republic), Centre National de la Recherche Scientifique, Commissariat à l'Énergie Atomique, and Institut National de Physique Nucléaire et de Physique des Particules (France), Bundesministerium für Bildung und Forschung, Deutscher Akademischer Austausch Dienst, and Alexander von Humboldt Stiftung (Germany), Hungarian National Science Fund, OTKA (Hungary), Department of Atomic Energy and Department of Science and Technology (India), Israel Science Foundation (Israel), National Research Foundation and WCU program of the Ministry Education Science and Technology (Korea), Physics Department, Lahore University of Management Sciences (Pakistan), Ministry of Education and Science, Russian Academy of Sciences, Federal Agency of Atomic Energy (Russia), VR and Wallenberg Foundation (Sweden), the U.S. Civilian Research and Development Foundation for the Independent States of the Former Soviet Union, the Hungarian American Enterprise Scholarship Fund, and the U.S.–Israel Binational Science Foundation.

-
- [1] R.L. Jaffe and A. Manohar, *Nucl. Phys.* **B337**, 509 (1990).
 - [2] X.-S. Chen, W.-M. Sun, F. Wang, and T. Goldman, *Phys. Lett. B* **700**, 21 (2011).
 - [3] Y. Hatta, *Phys. Rev. D* **84**, 041701 (2011).
 - [4] X. Ji, J.-H. Zhang, and Y. Zhao, *Phys. Rev. Lett.* **111**, 112002 (2013).
 - [5] M. Wakamatsu, *Phys. Rev. D* **85**, 114039 (2012).
 - [6] J. Ashman *et al.* (European Muon Collaboration), *Nucl. Phys.* **B328**, 1 (1989).
 - [7] B. Adeva *et al.* (Spin Muon Collaboration), *Phys. Rev. D* **58**, 112002 (1998).
 - [8] K. Abe *et al.* (E143 Collaboration), *Phys. Rev. D* **58**, 112003 (1998).
 - [9] D. de Florian, R. Sassot, M. Stratmann, and W. Vogelsang, *Phys. Rev. Lett.* **101**, 072001 (2008).
 - [10] D. de Florian, R. Sassot, M. Stratmann, and W. Vogelsang, *Phys. Rev. D* **80**, 034030 (2009).
 - [11] E. Leader, A. V. Sidorov, and D. B. Stamenov, *Phys. Rev. D* **82**, 114018 (2010).
 - [12] J. Blümlein and H. Böttcher, *Nucl. Phys.* **B841**, 205 (2010).
 - [13] M. Hirai and S. Kumano, *Nucl. Phys.* **B813**, 106 (2009).
 - [14] M.G. Alekseev *et al.* (COMPASS Collaboration), *Phys. Lett. B* **693**, 227 (2010).
 - [15] A. Airapetian *et al.* (HERMES Collaboration), *Phys. Lett. B* **666**, 446 (2008).
 - [16] A. Adare *et al.* (PHENIX Collaboration), *Phys. Rev. D* **76**, 051106 (2007).
 - [17] A. Adare *et al.* (PHENIX Collaboration), *Phys. Rev. D* **83**, 032001 (2011).
 - [18] L. Adamczyk *et al.* (STAR Collaboration), *Phys. Rev. D* **86**, 032006 (2012).
 - [19] S. S. Adler *et al.* (PHENIX Collaboration), *Phys. Rev. Lett.* **98**, 012002 (2007).
 - [20] A. Adare *et al.* (PHENIX Collaboration), *Phys. Rev. Lett.* **103**, 012003 (2009).
 - [21] A. Adare *et al.* (PHENIX Collaboration), *Phys. Rev. D* **87**, 012011 (2013).
 - [22] A. Adare *et al.* (PHENIX Collaboration), *Phys. Rev. D* **79**, 012003 (2009).
 - [23] B. I. Abelev *et al.* (STAR Collaboration), *Phys. Rev. Lett.* **100**, 232003 (2008).

- [24] D. de Florian, R. Sassot, and M. Stratmann, *Phys. Rev. D* **76**, 074033 (2007).
- [25] C. A. Aidala, F. Ellinghaus, R. Sassot, J. P. Seele, and M. Stratmann, *Phys. Rev. D* **83**, 034002 (2011).
- [26] S. S. Adler *et al.* (PHENIX Collaboration), *Phys. Rev. C* **75**, 024909 (2007).
- [27] H. Hahn *et al.*, *Nucl. Instrum. Methods Phys. Res., Sect. A* **499**, 245 (2003).
- [28] I. Nakagawa *et al.*, *Eur. Phys. J. Spec. Top.* **162**, 259 (2008).
- [29] A. Zelenski *et al.*, *Nucl. Instrum. Methods Phys. Res., Sect. A* **536**, 248 (2005).
- [30] RHIC Polarimetry Group, BNL Internal Note No. C-A/AP/490 (2013) [<http://public.bnl.gov/docs/cad/Documents/RHIC%20polarization%20for%20Runs%209-12.pdf>].
- [31] K. Adcox *et al.*, *Nucl. Instrum. Methods Phys. Res., Sect. A* **499**, 469 (2003).
- [32] W. Anderson *et al.*, *Nucl. Instrum. Methods Phys. Res., Sect. A* **646**, 35 (2011).
- [33] J. Beringer *et al.* (Particle Data Group), *Phys. Rev. D* **86**, 010001 (2012).
- [34] L. Aphecetche *et al.*, *Nucl. Instrum. Methods Phys. Res., Sect. A* **499**, 521 (2003).
- [35] A. Adare *et al.* (PHENIX Collaboration), *Phys. Rev. D* **88**, 032006 (2013).
- [36] A. Manion and A. Deshpande *et al.* (PHENIX Collaboration), *RIKEN Accel. Prog. Rep.* **43**, 72 (2010).
- [37] M. Glück, E. Reya, M. Stratmann, and W. Vogelsang, *Phys. Rev. D* **63**, 094005 (2001).
- [38] R. D. Ball S. Forte, A. Guffanti, E. R. Nocera, G. Ridolfi, and J. Rojo (NNPDF Collaboration), *Nucl. Phys.* **B874**, 36 (2013).
- [39] R. D. Ball *et al.* (NNPDF Collaboration), *Nucl. Phys.* **B867**, 244 (2013).
- [40] A. Vogt, *Comput. Phys. Commun.* **170**, 65 (2005).
- [41] B. Jäger, A. Schäfer, M. Stratmann, and W. Vogelsang, *Phys. Rev. D* **67**, 054005 (2003).
- [42] J. Pumplin, D. R. Stump, J. Huston, H. L. Lai, P. M. Nadolsky, and W. K. Tung, *J. High Energy Phys.* **07** (2002) 012.
- [43] E. R. Nocera, *Proc. Sci.*, DIS2013 (2013) 211.
- [44] J. R. Stevens *et al.* (STAR Collaboration), *Nuovo Cimento Soc. Ital. Fis.* **36C**, 39 (2013).